



**Abstract**

Previous geodetic and teleseismic observations of the 2021  $M_w$ 7.4 Maduo earthquake imply surprising but difficult-to-constrain complexity, including rupture across multiple fault segments and supershear rupture. Here, we present an integrated analysis of multi-fault 3D dynamic rupture models, high-resolution optical correlation analysis, and joint optical-InSAR slip inversion. Our preferred model, validated by the teleseismic multi-peak moment rate release, includes unilateral eastward double-onset supershear speeds and cascading rupture dynamically triggering two adjacent fault branches.

We propose that pronounced along-strike variation in fracture energy, complex fault geometries, and multi-scale variable prestress drives this event's complex rupture dynamics. We illustrate how supershear transition has signatures in modeled and observed off-fault deformation. Our study opens new avenues to combine observations and models to better understand complex earthquake dynamics, including local and potentially repeating supershear episodes across immature faults or under heterogeneous stress and strength conditions, which are potentially not unusual.

**Plain Language Summary**

The mechanism of cascading rupture and supershear propagation, when fault moves faster than *in situ* shear wave speed on multiple fault segments, remains unclear. On May 22, 2021, a magnitude 7.4 strike-slip earthquake occurred in central-east Tibet with episodic supershear suggested by geodetic and seismological inversions. Here, we build a physics-based 3D fully dynamic model, informed by regional tectonics, geomorphology, and high-resolution geodetic data, to better understand the earthquake's behavior and its implications for seismic hazards. The preferred rupture scenario reproduces key features, such as multi-peak moment release, asymmetric supershear fronts, and dynamic triggering of secondary fault branches. Our model suggests that regional stress field, geometric complexity, and the along-strike variation of frictional properties are crucial for earthquake dynamics and coseismic surface damage patterns. Our mechanically-viable model offers insights into a comprehensive knowledge of rupture complexity and regional seismic hazard assessment.

**1 Introduction**

On May 22, 2021, the Maduo earthquake, a  $M_w$ 7.4 strike-slip event, struck the northeastern Tibetan Plateau (Figure 1A), affecting the local population (UNICEF China, 2021) and infrastructure (e.g., M. Zhu et al., 2023). The earthquake ruptured the eastern segment of the Kunlun Mountain Pass–Jiangcuo Fault (KMPJF), a NW-trending left-lateral strike-slip branch fault south of the East Kunlun fault bounding the Bayan Har Block (Guo et al., 2021). The 2021 Maduo event is the largest earthquake in China since the 2008  $M_w$ 7.9 Wenchuan earthquake (Figure 1A) and resulted in complex surface rupture (Pan et al., 2022; Z. Yuan et al., 2022).

The major strike-slip faults surrounding the Bayan Har block all hosted large earthquakes with magnitudes  $>6.5$  in China since 1997 (L. Huang et al., 2021; P. Zhang et al., 2003; Y. Zhu et al., 2021). In contrast, no major earthquake occurred on the KMPJF, which does not have a clear geomorphological expression and was only partly mapped before the Maduo earthquake (Z. Yuan et al., 2022).

Previous studies focused on analyzing the static, kinematic, and dynamic source properties of the Maduo earthquake using geodetic, teleseismic, and field data (Gao et al., 2021; Jin & Fialko, 2021; Ren et al., 2021; L. He et al., 2021; Guo et al., 2021; Pan et al., 2022; Yue et al., 2022; J. Yuan & Li, 2023). Most joint inversions, combining geodetic and teleseismic observation, agree on the earthquake breaking across multiple fault

70 segments with varying rupture speeds (e.g., Yue et al., 2022; K. He et al., 2021; Jin &  
71 Fialko, 2021; S. Wang et al., 2022). The rupture speed inferred for the eastward-propagating  
72 front falls in the range of 3–5 km/s (Yue et al., 2022; X. Zhang et al., 2022; Q. Li et al.,  
73 2022) whereas the westward propagation is inferred as 2.5–2.8 km/s (Chen et al., 2022;  
74 Wei et al., 2022). However, the mechanical relationship between potential supershear rup-  
75 ture episodes and regional tectonics remains highly debated, partially due to the non-  
76 uniqueness of the results from various data-driven and physics-based models (Chen et  
77 al., 2022; Yue et al., 2022; X. Zhang et al., 2022; Wei et al., 2022; Fan et al., 2022).

78 Geometrically complex fault systems, such as the KMPJF, are expected to host  
79 smaller and slower earthquakes compared to more mature faults (Cappa et al., 2014; Manighetti  
80 et al., 2015; Y. Huang et al., 2014; Perrin et al., 2016), rendering the magnitude and in-  
81 ferred kinematic complexity of the Maduo earthquake surprising. This complexity re-  
82 peats in the coseismic surface damage distribution, constrained by geodetic observations  
83 (C. Li, Li, Shan, & Zhang, 2023; C. Li, Li, Hollingsworth, et al., 2023) and field mea-  
84 surements (Z. Yuan et al., 2022). The details of the surface rupture expression may cor-  
85 relate with subsurface rupture dynamics, multi-fault interaction, fault orientation with  
86 respect to the regional stress-field and near-fault plasticity (Wollherr et al., 2019; Jara  
87 et al., 2021; Taufiqurrahman et al., 2023; Rodriguez Padilla & Oskin, 2023; Wen et al.,  
88 2024; Liu-Zeng et al., 2024).

89 Together with a new analysis of high-resolution optical SPOT-6/7 data, the 2021  
90 Maduo earthquake provides a unique opportunity to understand the underlying physics  
91 of multi-segment bilateral rupture across a complex fault system and related observables.  
92 We demonstrate that combining high-resolution optical and InSAR data analysis with  
93 3D multi-fault dynamic rupture simulations can constrain dynamically viable pre- and  
94 co-seismic fault system mechanics and help reduce the non-uniqueness in earthquake source  
95 observations.

96 Our study combines 3D dynamic rupture simulations with joint optical and InSAR  
97 geodetic source inversion and surface damage measurements. The simulations incorpo-  
98 rate optically-derived multi-segment non-planar fault geometry, data-constrained het-  
99 erogeneous initial stress, off-fault Drucker-Prager plasticity, strong velocity-weakening  
100 rate-and-state friction, topography, and 3D subsurface velocity structure. Our preferred  
101 model reproduces the observed characteristics of the Maduo earthquake, such as multi-  
102 peak moment rate release, heterogeneous fault slip distribution, and multi-fault rupture.  
103 We compare the modeled co-seismic distribution of off-fault deformation with fault dam-  
104 age from surface geodetic measurements and identify geodetic off-fault signatures of su-  
105 pershear rupture onset. We illustrate the importance of key model ingredients by con-  
106 trasting them with less optimal rupture scenarios. We propose that along-strike varia-  
107 tions in fracture energy and fault geometry and 3D variable multi-scale prestress gov-  
108 ern the complex multi-segment rupture dynamics and favor unilateral double-onset su-  
109 pershear propagation.

## 110 2 Methods

### 111 2.1 Geodetic analysis

112 We perform joint InSAR (Sentinel-1 imagery) and optical geodetic analysis of the  
113 Maduo earthquake. We measure the horizontal surface displacement field from the cor-  
114 relation of high-resolution SPOT-6/7 satellite imagery (Figure 1B, Supporting Informa-  
115 tion S2). This allows us to map the surface rupture traces and analyze the pattern of  
116 near-fault deformation. We infer a main segment (F1 in Figure 1B) connected to a shorter  
117 segment (F2) via a restraining step-over and a third smaller segment (F3), branching south-  
118 eastward from the main segment. We measure the amount and variability of surface fault  
119 slip and fault zone width from stacked perpendicular profiles of the SPOT-6/7 surface

120 displacement field, regularly spaced along the fault strike (Supporting Information S2).  
 121 Assuming a homogeneous elastic half-space, we combine Sentinel-2 optical data at a res-  
 122 olution of 40 m with InSAR data to infer the static slip distribution at depth from a con-  
 123 strained least-square inversion (Supporting Information S2, Figures S4-S7). Here, all faults  
 124 are assumed 83°N dipping for simplicity (Figure S4).

## 125 2.2 3D dynamic rupture simulations

126 We simulate 3D dynamic rupture across multiple fault segments and the associ-  
 127 ated seismic wave propagation using the open-source software *SeisSol* (Käser & Dumber-  
 128 ser, 2006; Pelties et al., 2014; Heinecke et al., 2014; Uphoff et al., 2017, Supporting In-  
 129 formation S1). Dynamic rupture models require initial conditions, including fault geom-  
 130 etry, prestress, frictional fault strength, and subsurface elastic and plastic material prop-  
 131 erties (Harris et al., 2018; Ramos et al., 2022; A. Gabriel et al., 2023).

132 We construct the fault geometry by extruding the geodetically inferred surface fault  
 133 traces at depth, assuming variable dip angles constrained from relocated aftershock dis-  
 134 tributions (W. Wang et al., 2021). Our constructed fault geometries agree with most kine-  
 135 matic source models that assume a main fault dipping northward and two sub-vertical  
 136 eastern branches (Chen et al., 2022; Jin & Fialko, 2021; W. Wang et al., 2021; Fan et  
 137 al., 2022). In our preferred dynamic rupture model, we assume a northward-dipping an-  
 138 gles of 83° for the main fault segment (Chen et al., 2022; Yue et al., 2022), and 85° south  
 139 for the segments F2 and F3. Segment F2 is shallowly connected to the main segment,  
 140 while F3 is disconnected.

141 Our assumed prestress is depth-dependent and multi-scale; we combine a laterally  
 142 uniform ambient tectonic loading resembling the regional stress state with geodetically  
 143 constrained small-scale on-fault stress heterogeneities and depth-dependent normal stress.  
 144 The resulting combined on-fault and off-fault initial shear and normal stress distribu-  
 145 tion are heterogeneous on the scale of the non-planar fault geometry.

146 We set a uniform non-Andersonian homogeneous background stress orientation (Fig-  
 147 ure S2) guided by regional moment tensor inversion (B. Xu & Zhang, 2023). This pre-  
 148 stress resembles sinistral strike-slip faulting with the maximum compressive stress di-  
 149 rection  $S_{Hmax} = N78^\circ E$  and the stress shape ratio  $\nu = 0.5$ . We assume depth-dependent  
 150 effective normal stresses following a hydrostatic gradient characterized by a pore fluid-  
 151 pressure ratio of  $\gamma = \rho_{water}/\rho_{rock} = 0.37$  (Supporting Information S1, Figure S3A).  
 152 While all fault segments vertically extend to 20 km depth, we mimic the brittle-ductile  
 153 transition at  $\approx 10$  km by smoothly reducing deviatoric stresses to zero (Figure S3B, Ul-  
 154 rich et al., 2019).

155 In addition to the regional ambient prestress, which is modulated by the non-planar  
 156 fault geometry (e.g., Biemiller et al., 2022), we add small-scale prestress variability in-  
 157 ferred from our geodetic slip model (Supporting Information text S1, Tinti et al., 2021;  
 158 Jia et al., 2023). The geodetically inferred prestress variability enhances the shear stresses  
 159 in optimally oriented portions of the fault by a maximum of  $\approx 3$  MPa within the seis-  
 160 mogenic zone (Figure S2A). It also reduces the shear stress at strong geometrical bends  
 161 by  $\approx 1$  MPa, while generally increasing the normal stresses up to 2.9 MPa on F3 (Fig-  
 162 ure S2B).

163 A fast velocity-weakening rate-and-state friction law governs the strength of all faults  
 164 (Dunham et al., 2011b; A.-A. Gabriel et al., 2012). All friction parameters are listed in  
 165 Table S1. We include a 1 km shallow velocity-strengthening layer (Figure S1E) in agree-  
 166 ment with the observed early afterslip (Jin & Fialko, 2021; Jin et al., 2023).

167 The  $S$  parameter (Andrews, 1976; Aki & Richards, 2002; Dunham, 2007) charac-  
 168 terizes the relative fault strength governing dynamic rupture propagation and arrest by

balancing fracture energy and strain energy release (Cocco et al., 2023). It is defined as the ratio between the peak and residual strengths,  $\tau_p$  and  $\tau_r$  relative to the background level of initial loading  $\tau_0$ , so that  $S = (\tau_p - \tau_0)/(\tau_0 - \tau_r)$ . In our framework, complex initial stress and fault geometries modulate the closeness to failure before the onset of rupture and the relative fault strength.

We account for regional 3D high-resolution velocity structure (Xin et al., 2018), with a resolution of 0.5 degrees laterally and 5 km resolution with depth (Figure S1D). We include off-fault plasticity described by non-associative Drucker-Prager visco-plastic rheology (Andrews, 2005; Wollherr et al., 2018). We use a bulk friction coefficient of 0.5 and a bulk plastic cohesion  $C_{off}$  proportional to the 3D variable shear modulus  $\mu$  as  $C_{off} = 2 \times 10^{-4} \mu$  (Table S1) throughout the entire domain (Roten et al., 2014; Taufiqurrahman et al., 2023). The volumetric bulk initial stresses governing off-fault plasticity are the same as the depth-dependent, laterally uniform ambient tectonic prestress.

### 3 Results

#### 3.1 Heterogeneous near-surface deformation and homogeneous fault slip at depth from joint geodetic analysis

The 6 m resolution SPOT 6/7 fault-parallel displacement field shown in Figure 1B reveals a highly heterogeneous deformation pattern along the rupture trace. Deformation ranges from very localized ( $<0.6$  km), i.e., sharp discontinuities in the surface displacement field in the vicinity of the fault, to broader shear zones ( $>1.8$  km), i.e., more gradual displacement changes across a wider fault zone (Figure S25). This is reflected in strong variations of our measured fault zone width along strike (Figure 1B).

Westward of the epicenter, surface deformation can be divided into two distinct regions: (i) a 30 km long segment where deformation is broadly distributed, characterized by an average fault zone width of 1538 m; (ii) a 40 km segment at the western end of the rupture, where deformation is highly localized, and the mean fault zone width is 425 m. Eastward of the epicenter, surface deformation is more heterogeneous. We identify three areas of localized deformation with a mean fault zone width of 747 m, 587 m, and 568 m, from west to east, respectively. These are separated by two areas of distributed deformation with a mean fault zone width of 1660 m and 1213 m, respectively.

We infer considerable surface fault offsets (Figure 1B) of 2.44 m on average. The fault offsets tend to be larger where deformation is localized. However, there are exceptions, e.g., near latitude  $98.65^\circ\text{E}$ . We identify three distinct regions of high surface slip located at the western and eastern ends of the rupture surface expression, respectively, and near longitude  $98.65^\circ\text{E}$ .

Our joint InSAR Sentinel-1 and optical Sentinel-2 geodetic slip model is shown in Figure 2C and features overall smooth, shallow ( $<10$  km depth) and high-amplitude fault slip, in agreement with previous geodetic and teleseismic slip models (e.g., Jin & Fialko, 2021; Q. Li et al., 2022). We resolve three areas of large slip reaching 6 m and a significant dip-slip component at the western end of fault segment F1. Slip across segment F3 is, on average, lower and shallower than for the two main fault segments, F1 and F2.

We use our joint geodetic analysis to inform and verify a suite of dynamic rupture simulations. Subsequently, we discuss signatures of rupture complexity in the on- and off-fault geodetic data.

214

### 3.2 Multi-fault 3D dynamic rupture scenarios

215

216

217

218

219

220

221

To find a preferred rupture scenario, we explore an ensemble of more than 100 dynamic rupture scenarios varying fault fracture energy, off-fault material strength, prestress, and fault segmentation. We initiate all rupture scenarios at the USGS hypocentre (Supporting Information S1). Our preferred model features cascading dynamic rupture across multiple segments and double-onset, unilateral supershear along the eastern faults (Figure 2). It matches key observed characteristics of the event, including the multi-peak moment rate release and the overall on-fault slip distribution (Figure 2A,B).

222

223

224

225

226

227

228

229

Figure 2A compares the dynamic rupture moment rate release with teleseismic inferences by the USGS and Chen et al. (2022). Our preferred model has a total seismic moment of  $0.98 \times 10^{20}$  N m, equivalent to an on-fault moment magnitude of  $M_w 7.26$ . Our modeled on-fault moment rate release resembles the two major peaks of the USGS source time function at 13 and 20 s, within the expected uncertainties. Overall, the teleseismic inferences have a slightly longer duration, which may be attributed to differences between our on-fault model results and teleseismic inferences, assumed fault geometries and velocity structure, source time functions, and resolution differences.

230

231

232

233

234

Our dynamic model results in an average slip  $\approx 1.5$  m larger than the static model (Figures 1C, 2B,C). We observe three sub-regions of high slip accumulation (Figures 1C, 2B), two on the main branch with a maximum slip of 5.2 m and 4.8 m, 37 km west and 11 km east of the hypocenter respectively, while the third high slip patch is located on F2 with a max slip of 4.8 m, 40 km east of the hypocenter.

235

236

237

238

239

240

241

242

243

244

245

246

247

248

249

250

251

252

253

254

255

256

Figures 2D,E show rupture velocity on the fault and at 3.5 km depth. Spontaneous rupture propagates bilaterally to the northwest and southeast (Figure 2F). While there is limited along-strike variability in seismic wave speeds given by the velocity model, rupture speed varies significantly. The westward rupture front travels at an average speed of  $2.77 \text{ km s}^{-1}$  for 24 s before arresting the edge of the main fault F1 (Figure 2D,E,F). We observe early, transient supershear to the west, which is not self-sustained but leads to higher shallower rupture velocities from 12 km to 30 km west to the hypocenter at shallow depths ( $< 1.9$  km, Figure 2D). The eastward propagating rupture front transitions to supershear speeds twice along the main fault and after “jumping” to fault segment F2 (Figure 2D). At rupture onset, the eastward rupture speed is slightly slower than the westward one with  $2.59 \text{ km s}^{-1}$ , being delayed due to a non-optimally oriented fault bend at the Eastern segment (Fig. S1). After  $\approx 10$  s, the rupture accelerates to  $4.30 \text{ km s}^{-1}$  which is close to the local P-wave speed ( $4.48 \text{ km s}^{-1}$ , Figure 2E). The first transition from subshear to sustained supershear rupture occurs when the rupture front breaks through the free surface 8 km east of the hypocenter (Figures 2D,F). The surface rupture initiates a supershear transition by P-wave diffraction at the free surface (e.g., Kaneko & Lapusta, 2010; J. Xu et al., 2015; Hu et al., 2021; Tang et al., 2021). The supershear rupture front then dynamically triggers coseismic slip on F2 and F3 at about 14 and 18.5 s, respectively (Figure 2F). The second eastward supershear transition occurs soon after the onset of rupture on F2 at about 45 km along strike from the epicenter (Figure 2D). Eastward rupture then arrests when reaching the eastern end of the third branch at 28 s (Figure 2F).

257

258

259

260

261

262

263

264

265

We find that a decrease in characteristic slip distance  $D_{RS}$  for 20 km along-strike the eastern main fault away from the hypocenter (Figure S1F) is required to facilitate dynamic triggering of the southernmost fault branches F2 and F3. In our preferred model, the relatively high prestress around the nucleation area promotes initial supershear fronts in both directions, while only the propagating front along the eastern fault sustains. There, locally lower  $D_{RS}$  decreases fracture energy (Cocco et al., 2023), favors supershear rupture speeds, and increases dynamically accumulating fault slip. In Figures S9, S11, we show alternative models with homogeneously small and large  $D_{RS}$  leading to either bilateral sub- or bilateral supershear rupture, respectively (Supplementary Information text

266 S4). Both models fail to rupture all fault segments and cannot reproduce neither the char-  
 267 acteristic moment rate release peaks nor their duration. Furthermore, both models gen-  
 268 erate large off-fault plasticity in the western section of the fault system, which does not  
 269 compare well to observations (section 3.3, Figures 3, S10, S12).

270 We illustrate the significance of incorporating off-fault plasticity to match the geode-  
 271 tically observed distribution of off-fault damage in Figures S14 and S16 (Supplementary  
 272 Information text S4). These alternative scenarios have lower and higher bulk plastic co-  
 273hesion, respectively, affecting the width of the off-fault plastic strain pattern and the rup-  
 274 ture energy budget. We illustrate the importance of fault geometries in two exemplary  
 275 alternative models with varying segmentation and dipping angles in Figures S17 and S19.  
 276 When F1 and F2 are modeled as a continuous segment, the rupture succeeds in dynam-  
 277 ically activating F3. However the off-fault plastic strain pattern changes towards the east-  
 278 ernmost branches (Supplementary Information Text S5). In contrast, segments F2 and  
 279 F3 are not rupturing in an alternative model where these segments are not continuous  
 280 but dip  $83^\circ$  northward (Figure S19).

281 The initial conditions of our preferred dynamic rupture model yield highly hetero-  
 282 geneous relative fault strength, as illustrated by the on-fault variability of the  $S$  param-  
 283 eter (Figure S1I). Regions of low  $S < 1.2$  characterize the southeastern faults, facili-  
 284 tating dynamic triggering of the adjacent segments F2 and F3 and favoring local super-  
 285 shear rupture velocities. Several locally stronger fault portions act as barriers, as indi-  
 286 cated by higher  $S$  values in the eastern part of the fault system. Figures S21 and S23  
 287 show alternative models with different choices for the ambient stress orientation (Sup-  
 288 plementary Information text S6). A smaller  $S_{Hmax}$  angle ( $S_{Hmax} \approx N68^\circ E$ ) yields larger  
 289 slip along the F1 and F2 segments (Fig. S21), larger simulated offsets, and larger off-  
 290 fault deformation at the eastern segments of the fault system (Fig. S22) compared to  
 291 the preferred model. Larger  $S_{Hmax}$  orientation ( $S_{Hmax} \approx N88^\circ E$ ) results in longer rup-  
 292 ture duration and uniformly subshear rupture speeds, reduced on-fault slip, off-fault plas-  
 293 tic strain, and simulated offsets, and the inability to dynamically trigger F3 (Fig. S23).

### 294 3.3 Modeled off-fault deformation

295 Our dynamically modeled surface deformation matches the GPS observations (M. Wang  
 296 et al., 2021), although the horizontal components are slightly underestimated (Figure  
 297 S26A-B). We observe the largest misfit in orientation and amplitude at station QHAJ,  
 298 potentially due to unmodelled local fault zone structures. Our preferred forward sim-  
 299 ulation also reproduces the surface deformation inferred from both the ascending and  
 300 descending interferograms, with minor divergence near the fault trace (Figure S26C-H).

301 Figure 3A shows a map view and 3D cross-sections of the plastic strain accumu-  
 302 lated during the dynamic rupture simulation. The surface distribution of off-fault plas-  
 303 tic deformation varies along strike, with a wider distribution observed further away from  
 304 the epicenter and significant local variations. Analyzing the modeled plastic strain along  
 305 fault-perpendicular transects (Figure 3B and Supporting Information Text S3) reveals  
 306 two zones of reduced deformation width located at  $97.85^\circ E$ - $98.15^\circ E$  and  $98.25^\circ E$ - $98.45^\circ E$   
 307 (inset b in Figure 3A and Figure 3B). These zones are separated by local peaks in off-  
 308 fault plastic deformation corresponding to fault geometrical complexities such as fault  
 309 kinks and intersections (insets a, c, and e in Figure 3A). In addition, we observe that the  
 310 plastic strain distribution is strongly asymmetric across the fault. A higher level of plas-  
 311 tic strain is observed on the northern part of segment F1, although 3D cross-sections c  
 312 and d show a subtle southward asymmetry (Figure 3A). In contrast, the modeled off-  
 313 fault deformation localizes toward the south across segment F2.

## 314 4 Discussion

### 315 4.1 Unilateral supershear and cascading dynamic rupture

316 The observational evidence for supershear rupture during the Maduo event remains  
 317 debated. Several studies report asymmetric rupture with supershear velocity to the east  
 318 from kinematic finite fault inversion and back-projection analysis (Yue et al., 2022; X. Zhang  
 319 et al., 2022; Q. Li et al., 2022; Lyu et al., 2022). However, bilateral transient supershear  
 320 episodes have also been inferred using similar methodologies and datasets (Cheng et al.,  
 321 2023; B. Xu & Zhang, 2023). Wei et al. (2022) argue for sustained subshear speed of the  
 322 entire rupture from back-projection and multiple point source inversion, which is in line  
 323 with the joint geodetic and teleseismic inversion of Chen et al. (2022). Our geodetically  
 324 constrained dynamic rupture simulations indicate energetic nucleation and eastward uni-  
 325 lateral, cascading supershear rupture speeds with a double transition from sub- to su-  
 326 pershear speeds that would complicate observational inferences. The model's average east-  
 327 ward supershear and westward subshear speeds of  $\sim 3.4 \text{ km s}^{-1}$  and  $\sim 2.18 \text{ km s}^{-1}$ , respec-  
 328 tively, fall within the range of observational values ( $2.82\text{--}5 \text{ km s}^{-1}$  and  $2\text{--}3 \text{ km s}^{-1}$ , re-  
 329 spectively, Yue et al., 2022; X. Zhang et al., 2022; Q. Li et al., 2022; Lyu et al., 2022).

330 Cascading spontaneous rupture dynamically triggering both southeastern fault branches  
 331 is a key constraint in identifying the dynamic parameters of our preferred simulation.  
 332 Our models suggest that the dynamic triggering of the eastern branches may not have  
 333 happened without an eastward supershear rupture front. We demonstrate that along-  
 334 fault variations in fracture energy can be a key driver of diverse ranges of rupture speeds  
 335 during the same earthquake. The second onset of eastward supershear rupture is also  
 336 located at the free surface but aided by dynamic rupture jumping across highly stressed  
 337 step-over faults of variable dip (Hu et al., 2016; Tang et al., 2021). Wen et al. (2024) an-  
 338 alyzed dynamic rupture models with realistic fault geometry and variable regional stresses  
 339 to demonstrate the impact of compressive stress orientation on fault slip, dynamic trig-  
 340 gering, and supershear propagation. Our simulations additionally integrate regional geode-  
 341 tic constraints (C. Li, Li, Shan, & Zhang, 2023; C. Li, Li, Hollingsworth, et al., 2023)  
 342 and explore the importance of frictional variability, small-scale heterogeneity in local fault  
 343 stress and complex off-fault rheology on coseismic rupture dynamics.

### 344 4.2 Geodetic off-fault signatures of rupture complexity

345 Quantifying the degree of localization of the near-fault deformation from fault zone  
 346 width (FZW) measurements can help unravel the mechanical behavior of the shallow crust.  
 347 However, interpretation of such data is difficult due to several mechanisms superimpos-  
 348 ing and producing similar off-fault deformation patterns (Nevitt et al., 2020). For ex-  
 349 ample, a wide optically inferred fault zone width can be interpreted either as the elas-  
 350 tic bulk response of a localized decrease of slip in the shallow part of the fault (i.e., the  
 351 shallow slip deficit, Fialko et al., 2005) or as distributed inelastic deformation (Milliner  
 352 et al., 2015; Antoine et al., 2021; Scott et al., 2018). In addition, a wide fault zone width  
 353 may also result from the shallow soil response to coseismic rupture.

354 Here, we compare our geodetic observations of distributed deformation through the  
 355 estimated FZW with the plastic strain distribution of our preferred dynamic rupture model.  
 356 In this model, off-fault plastic deformation is generally more widespread in the eastern  
 357 sections of the fault system due to the higher dynamic stresses induced by the supers-  
 358 hear rupture front (Dunham et al., 2011b; Jara et al., 2021). In addition, the plastic strain  
 359 is mainly located on the compressive side of the fault due to the shallow angle of the max-  
 360 imum compressive stress to the fault ( $\sim 20^\circ$ ) (Templeton & Rice, 2008); and is modu-  
 361 lated by the geometric fault strike variations (Dunham et al., 2011a; Wollherr et al., 2019).  
 362 The simulated distribution of plastic strain remains similar for different plasticity pa-  
 363 rameterizations (Supporting Information S4), while the amplitude of off-fault plastic strain  
 364 changes (Figure S14,S16).



Our comparison suggests that the optically inferred distributed deformation can be at least partially attributed to off-fault plastic deformation. The measured optical FZW and the modeled plastic deformation width show strikingly similar along-strike variability at several locations (Figure 3): (i) a narrow peak of enlarged fault zone width between  $98.20^\circ$  and  $98.25^\circ$ ; (ii) a 10 km long zone of large optical FZW centered on longitude  $98.60^\circ$  coinciding with a peak in the plastic deformation width; and (iii) three peaks in the amount of modeled off-fault plasticity on segment F2 correlating with three (less pronounced) peaks in the optical data.

The optical FZW and modeled plastic deformation width also show various disagreements. Near the epicenter, between  $98.3^\circ$  and  $98.45^\circ$ , the optical fault zone width is large, 1800 m on average, whereas our preferred model does not show widespread off-fault plastic deformation. At this particular location, the large optical FZW may partly be attributed to the local geomorphology, which is characterized by Quaternary sand-dunes and swampy terrain where deformation cannot easily localize (Z. Yuan et al., 2022). Moreover, this part of the fault experienced the largest shallow afterslip (Fang et al., 2022), suggesting that the large FZW inferred from our observations may be due to a deficit of shallow slip.

We interpret an observed drastic local reduction of optically inferred fault zone width as a possible geodetic signature of the first supershear transitions of the eastward propagating front. 2D numerical models have shown that the location of supershear transition can be associated with a sharp local reduction of the damage zone width (Templeton & Rice, 2008; Jara et al., 2021) due to the spatial contraction of the stress field around the rupture tip. In nature, this has been observed using optical data, albeit once only, for the 2001  $M_s$  7.8 Kunlun earthquake (Jara et al., 2021). The drastic and localized reduction of the optically-inferred fault zone width at  $98.5^\circ$  (Figures 1 and 3B) occurs at a straight portion of the fault and does not appear to correlate with variations in the subsurface material, but does correlate with the first onset of eastward supershear rupture propagation in our preferred dynamic rupture model. The reduction of the modeled off-fault plastic strain width is more gradual in our 3D model than in previous studies, which is likely due to the more gradual onset of supershear rupture at different fault depths (Fig. 2D).

Our results imply that a high level of fault maturity, as well as homogeneous stress-strength conditions and geometric simplicity, may not necessarily be required preconditions for supershear rupture. Local and potentially repeating supershear episodes across immature faults or under heterogeneous stress and strength conditions have been inferred for the 2023 Turkey earthquake doublet (Jia et al., 2023; Delouis et al., 2023; Abdelmeguid et al., 2023) and may be more common than previously thought.

A remarkable gap in aftershock seismicity (W. Wang et al., 2021) between  $98.65^\circ$  –  $98.9^\circ$  (Figure 3C) may provide additional evidence for eastward supershear propagation. Postseismic quiescence on supershear segments has been previously observed and may reflect comparably homogeneous strength-stress conditions on geometrically simple and mature faults (Bouchon & Karabulut, 2008; Bouchon et al., 2010). In sharp contrast, the Maduo earthquake’s gap of aftershocks encompasses a major step-over and several fault bends. While the second supershear transition also aligns with a gap in aftershocks, its signature is less clear in both optical data and our model, possibly due to the spatial proximity to geometric fault complexities.

The relative fault strength of our preferred scenario is highly heterogeneous ( $S$  ratio, Figure S11), with localized weak asperities and strong strength barriers. Moreover, the Jiangcuo fault that broke during the Maduo earthquake does not have a pronounced geomorphological expression and was only partly mapped before the occurrence of the event. Its cumulative long-term displacement has been measured at only two locations

416 and is low ( $<5$  km, C. Li, Li, Shan, & Zhang, 2023). The fault's low geodetic slip rates  
417 ( $1.2\pm 0.8$  mm/an, Y. Zhu et al., 2021) also suggest that this fault is likely immature.

## 418 5 Conclusion

419 We demonstrate that an integrated analysis of an ensemble of multi-fault 3D dy-  
420 namic rupture models, high-resolution optical correlation analysis, joint optical-InSAR-  
421 slip inversion, and validation by teleseismic observations can help to develop a funda-  
422 mental understanding of the mechanical conditions that may have governed the complex  
423 dynamics of the 2021  $M_w 7.4$  Maduo earthquake. We extract high-resolution surface rup-  
424 ture traces from optical correlation and invert for a static slip model using InSAR and  
425 optical data, providing information on small-scale fault heterogeneous stress. Our pre-  
426 ferred dynamic rupture model accounts for multi-segment fault geometry, varying dip  
427 angles along the fault, multi-scale stress heterogeneities, and variation in fault fracture  
428 energy. It can explain the event's complex kinematics, such as a multi-peak moment rate  
429 release, unilateral supershear rupture, and dynamic triggering of secondary branches. In  
430 the west, despite the smoother fault morphology, dynamic rupture does not transition  
431 to supershear in our preferred model. This may be attributed to insufficient stress ac-  
432 cumulation and local variations in fault friction properties, which might not favor su-  
433 pershear despite the smoother fault surface. In contrast, the unexpected transition to  
434 supershear in the east, sustained despite rupture jumping across the complex, more seg-  
435 mented fault system geometry, highlights the potential importance of fault heterogeneities  
436 and complex stress fields efficiently promoting supershear propagation under seemingly  
437 unfavorable conditions. We explore the sensitivity of rupture dynamics to fault segmen-  
438 tation, tectonic prestress, off-fault plasticity, and frictional fault parameters. By com-  
439 paring geodetic and dynamic rupture off-fault plastic damage measures, we identify ob-  
440 servational signatures of supershear rupture. Our results imply that a high level of fault  
441 maturity, as well as homogeneous stress-strength conditions and geometric simplicity,  
442 may not necessarily be required preconditions for supershear rupture. This study opens  
443 new avenues to observe and better understand such - potentially not unusual - complex  
444 earthquake dynamics and their underlying driving factors.

## 445 Acknowledgments

446 This work was supported by the European Union's Horizon 2020 research and in-  
447 novation programme (TEAR ERC Starting; grant no. 852992) and Horizon Europe (ChEESA-  
448 2P, grant no. 101093038; DT-GEO, grant no. 101058129; and Geo-INQUIRE, grant no.  
449 101058518), the National Science Foundation (grant nos. EAR-2225286, EAR-2121568,  
450 OAC-2139536, OAC-2311208), the National Aeronautics and Space Administration (grant  
451 no. 80NSSC20K0495).

## 452 Data and Code Availability

453 We use the SeisSol software package available on GitHub ([https://github.com/](https://github.com/SeisSol/SeisSol)  
454 [SeisSol/SeisSol](https://github.com/SeisSol/SeisSol)) to simulate all dynamic models. The procedure to download and run  
455 the code is described in the SeisSol documentation ([seissol.readthedocs.io/en/latest/](https://seissol.readthedocs.io/en/latest/)).  
456 The pseudo-dynamic simulation using a kinematic slip model on the fault to calculate  
457 fault stress heterogeneity is stated in the document ([https://seissol.readthedocs.io/](https://seissol.readthedocs.io/en/latest/slip-rate-on-DR.html)  
458 [en/latest/slip-rate-on-DR.html](https://seissol.readthedocs.io/en/latest/slip-rate-on-DR.html))

459 The authors declare that all data supporting the findings of this study are avail-  
460 able within the paper and its Methods section. In particular, all data required to repro-  
461 duce the earthquake scenario can be downloaded from [https://drive.google.com/file/](https://drive.google.com/file/d/1rtZSWG1YQ-I-Czn5eZSNJKSyVG4dU_gU/view?usp=sharing)  
462 [d/1rtZSWG1YQ-I-Czn5eZSNJKSyVG4dU\\_gU/view?usp=sharing](https://drive.google.com/file/d/1rtZSWG1YQ-I-Czn5eZSNJKSyVG4dU_gU/view?usp=sharing).

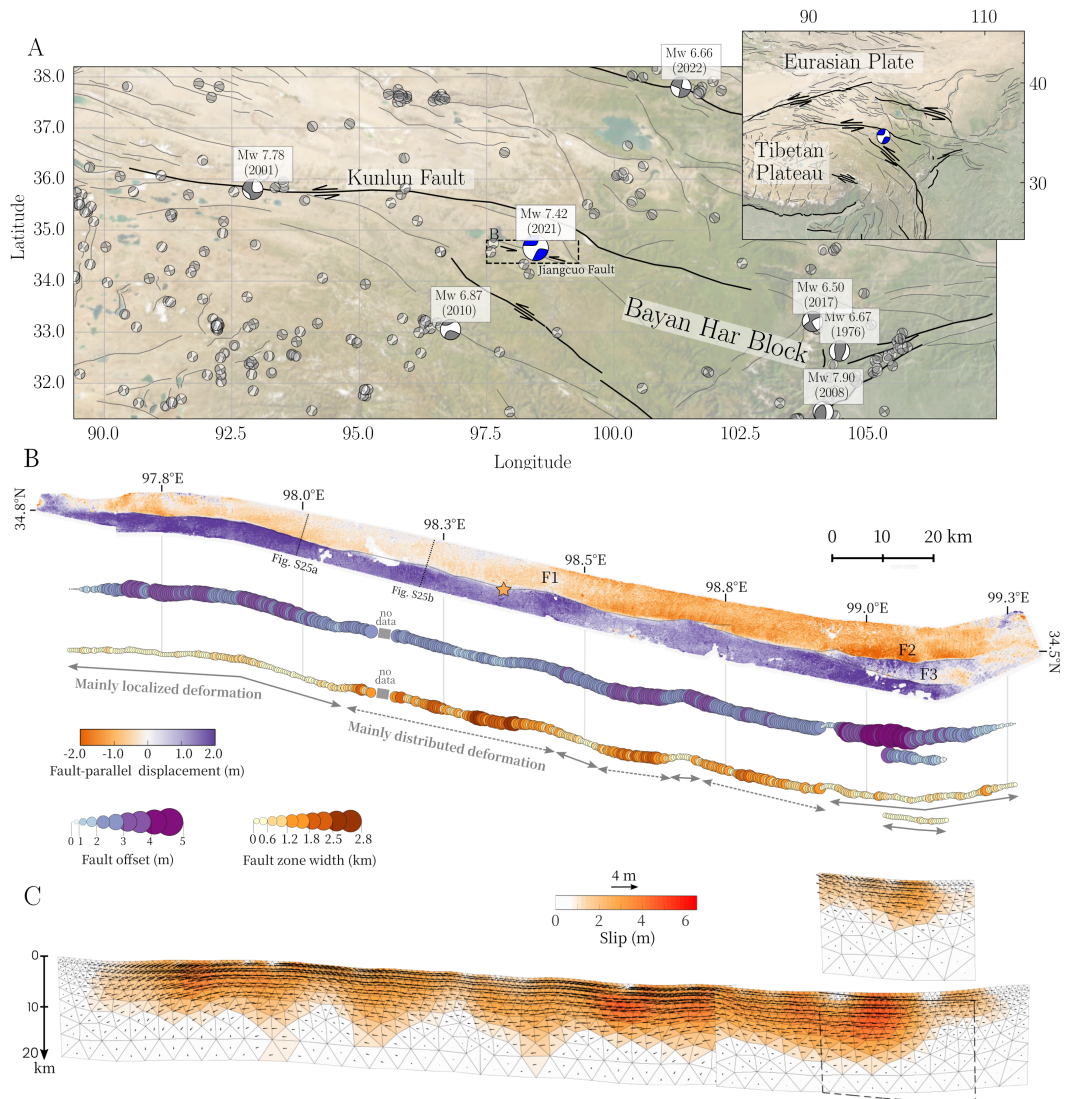


**Figure 1.** (A) Tectonic setting of the study area showing the regional active faults of the Tibetan Plateau (black lines, (Styron et al., 2010)) and the moment tensor mechanisms of past earthquakes (gray beachballs, extracted from the global Central Moment Tensor database (Dziewonski et al., 1981; Ekström et al., 2012)).  $M_w \geq 6.5$  focal mechanisms are labeled and highlighted using larger beachball diagrams. Superimposed is the 2021  $M_w 7.4$  Maduo earthquake USGS moment tensor mechanism (blue). The top-right inset shows a zoom-out view of the study area. (B) Top: Surface fault-parallel displacement field of the  $M_w 7.4$  Maduo event inferred from the correlation of SPOT-6 optical satellite imagery (Supplementary Information S2). The gray lines indicate the surface fault traces extracted from the fault-parallel displacement field and the dotted black lines locate the profiles shown in Figure S25. Middle and bottom: Fault offsets and fault zone width along the fault strike measured from the fault-parallel surface displacement field. (C) Slip amplitude and rake for the Maduo earthquake estimated from a joint inversion of InSAR and optical data. The assumed fault geometry comprises one main fault and two branching segments in the east, consistent with the dynamic rupture simulation.

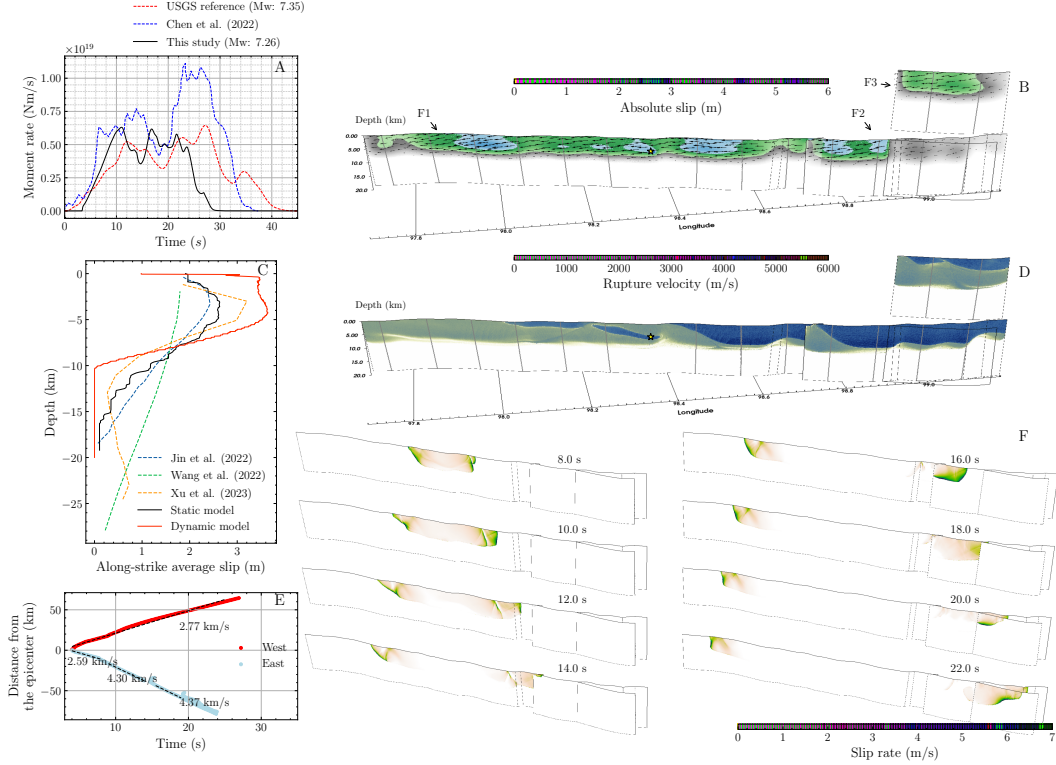


**Figure 2.** (A) Modeled moment rate function of the preferred dynamic rupture scenario for the 2021  $M_w$ 7.4 Maduo earthquake (black). The finite fault moment rate functions from USGS (2021) and Chen et al. (2022) are shown as red and blue dashed lines, respectively. (B) Modeled fault slip amplitude on the fault segments (F1, F2, and F3) in a three-dimensional perspective view. Fault slip along segment F3, which is located close to F2, is shown in the top inset. The vertical axis indicates the depth below the Plateau surface from 0 to 20 km. Black vectors indicate the slip direction of the rupture front (rake). Contour lines every 10 km from the epicenter are indicated as gray solid lines on the fault. (C) Comparison of the distribution of average slip with depth for our dynamic and static models as well as other published slip models. (D) Distribution of the rupture velocity on the fault. (E) Rupture times of westward and eastward propagating fronts against their distances from the epicenter, along a transect at 3.5 km depth. The rupture velocities estimated along different fault portions are indicated as dashed lines. (F) Snapshots of fault slip rate shown every two seconds between  $t=8.0$  s to  $t=22.0$  s of simulation time.

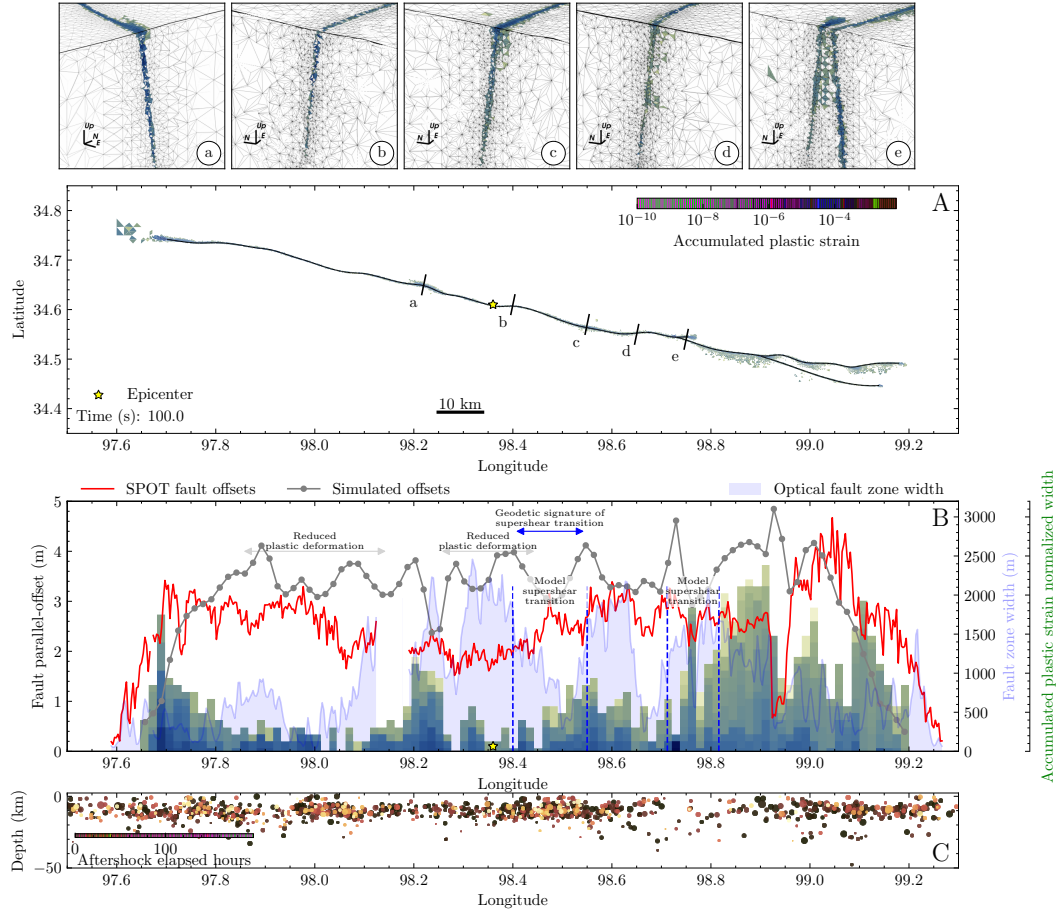


**Figure 3.** (A) Map view of the accumulated plastic strain at the surface at the end of the dynamic rupture simulation. The USGS epicenter is marked with a star. The top-panel insets (a-e) show a three-dimensional perspective view of the plastic strain accumulation at five chosen locations indicated by black lines in (A). (B) Comparison of the optically-inferred fault-parallel offsets (red) and fault zone width (shaded light blue area) with the simulated fault offsets (gray) and off-fault plasticity (histogram). The histogram depicts the along-strike variation of surface accumulated plastic strain derived from 94 transects along-strike composed of 100 sampling points over a width of 8.88 km. Vertical blue dashed lines mark the two supershear transitions in our preferred model while the horizontal blue line locates the signature of supershear transition in the optical data. (C) Depth versus longitude distribution of aftershocks from the catalog of W. Wang et al. (2021)

We use the following projection for the dynamic simulation: EPSG:3415. The Global Positioning System (GPS) three-component coseismic offsets used to compare with our dynamic rupture model synthetics are from M. Wang et al. (2021). The Sentinel-2 optical images are freely available and were downloaded from the European Space Agency website (<https://dataspace.copernicus.eu/>) SAR Copernicus Sentinel-1 data captured by ESA are freely available and were downloaded from PEPS archive operated by CNES <https://peps.cnes.fr/rocket/#/home>.

## Additional information

**Competing interests** The authors declare no competing interests.

## References

- Abdelmeguid, M., Zhao, C., Yalcinkaya, E., Gazetas, G., Elbanna, A., & Rosakis, A. (2023). Dynamics of episodic supershear in the 2023 M7.8 Kahramanmaraş/Pazarcik earthquake, revealed by near-field records and computational modeling. *Communications Earth & Environment*, 4(1), 456. doi: 10.1038/s43247-023-01131-7
- Aki, K., & Richards, P. G. (2002). *Quantitative seismology*.
- Andrews, D. J. (1976). Rupture propagation with finite stress in antiplane strain. *Journal of Geophysical Research (1896-1977)*, 81(20), 3575-3582. doi: 10.1029/JB081i020p03575
- Andrews, D. J. (2005). Rupture dynamics with energy loss outside the slip zone. *Journal of Geophysical Research: Solid Earth*, 110(B01307). doi: 10.1029/2004JB003191
- Antoine, S. L., Klinger, Y., Delorme, A., Wang, K., Bürgmann, R., & Gold, R. D. (2021). Diffuse deformation and surface faulting distribution from submetric image correlation along the 2019 Ridgecrest, California, ruptures. *Bulletin of the Seismological Society of America*, 111(5), 2275-2302.
- Biemiller, J., Gabriel, A.-A., & Ulrich, T. (2022). The Dynamics of Unlikely Slip: 3D Modeling of Low-Angle Normal Fault Rupture at the Mai'iu Fault, Papua New Guinea. *Geochemistry, Geophysics, Geosystems*, 23(5), e2021GC010298. Retrieved from <https://agupubs.onlinelibrary.wiley.com/doi/abs/10.1029/2021GC010298> (e2021GC010298 2021GC010298) doi: <https://doi.org/10.1029/2021GC010298>
- Bouchon, M., & Karabulut, H. (2008). The aftershock signature of supershear earthquakes. *Science*, 320(5881), 1323-1325. doi: 10.1126/science.1155030
- Bouchon, M., Karabulut, H., Bouin, M.-P., Schmittbuhl, J., Vallée, M., Archuleta, R., ... Marsan, D. (2010). Faulting characteristics of supershear earthquakes. *Tectonophysics*, 493(3-4), 244-253.
- Cappa, F., Perrin, C., Manighetti, I., & Delor, E. (2014). Off-fault long-term damage: A condition to account for generic, triangular earthquake slip profiles. *Geochemistry, Geophysics, Geosystems*, 15(4), 1476-1493.
- Chen, K., Avouac, J.-P., Geng, J., Liang, C., Zhang, Z., Li, Z., & Zhang, S. (2022). The 2021 Mw 7.4 Madoi earthquake: An archetype bilateral slip-pulse rupture arrested at a splay fault. *Geophysical Research Letters*, 49(2), e2021GL095243. doi: 10.1029/2021GL095243
- Cheng, C., Wang, D., Yao, Q., Fang, L., Xu, S., Huang, Z., ... Huang, X. (2023). The 2021 Mw 7.3 Madoi, China Earthquake: Transient Supershear Ruptures On a Presumed Immature Strike-slip Fault. *Journal of Geophysical Research: Solid Earth*, e2022JB024641. (e2022JB024641 2022JB024641) doi: <https://doi.org/10.1029/2022JB024641>
- Cocco, M., Aretusini, S., Cornelio, C., Nielsen, S. B., Spagnuolo, E., Tinti, E., & Di Toro, G. (2023). Fracture energy and breakdown work during earth-

- 514 quakes. *Annual Review of Earth and Planetary Sciences*, 51(1), 217-252. doi:  
515 10.1146/annurev-earth-071822-100304
- 516 Delouis, B., van den Ende, M., & Ampuero, J.-P. (2023). Kinematic rupture model  
517 of the February 6th 2023 Mw7. 8 Turkey earthquake from a large set of near-  
518 source strong motion records combined by GNSS offsets reveals intermittent  
519 supershear rupture. *Authorea Preprints*.
- 520 Dunham, E. M. (2007). Conditions governing the occurrence of supershear ruptures  
521 under slip-weakening friction. *Journal of Geophysical Research: Solid Earth*,  
522 112(B7). doi: 10.1029/2006JB004717
- 523 Dunham, E. M., Belanger, D., Cong, L., & Kozdon, J. E. (2011a). Earthquake  
524 ruptures with strongly rate-weakening friction and off-fault plasticity, part 2:  
525 Nonplanar faults. *Bulletin of the Seismological Society of America*, 101(5),  
526 2308–2322.
- 527 Dunham, E. M., Belanger, D., Cong, L., & Kozdon, J. E. (2011b). Earthquake Rup-  
528 tures with Strongly Rate-Weakening Friction and Off-Fault Plasticity, Part 1:  
529 Planar Faults. *Bulletin of the Seismological Society of America*, 101(5), 2296-  
530 2307. doi: 10.1785/0120100075
- 531 Dziewonski, A. M., Chou, T.-A., & Woodhouse, J. H. (1981). Determination of  
532 earthquake source parameters from waveform data for studies of global and  
533 regional seismicity. *Journal of Geophysical Research: Solid Earth*, 86(B4),  
534 2825-2852. doi: 10.1029/JB086iB04p02825
- 535 Ekström, G., Nettles, M., & Dziewoński, A. (2012). The global CMT project  
536 2004–2010: Centroid-moment tensors for 13,017 earthquakes. *Physics of the  
537 Earth and Planetary Interiors*, 200-201, 1-9. doi: 10.1016/j.pepi.2012.04.002
- 538 Fan, X., Zhang, G., Zhao, D., Xie, C., Huang, C., & Shan, X. (2022). Fault  
539 geometry and kinematics of the 2021 Mw 7.3 Maduo earthquake from af-  
540 tershocks and InSAR observations. *Frontiers in Earth Science*, 10. doi:  
541 10.3389/feart.2022.993984
- 542 Fang, J., Ou, Q., Wright, T. J., Okuwaki, R., Amey, R. M., Craig, T. J., ... Magh-  
543 soudi, Y. (2022). Earthquake cycle deformation associated with the 2021  
544 Mw 7.4 Maduo (Eastern Tibet) earthquake: An intrablock rupture event on  
545 a slow-slipping fault from Sentinel-1 InSAR and teleseismic data. *Journal of  
546 Geophysical Research: Solid Earth*, 127(11), e2022JB024268.
- 547 Fialko, Y., Sandwell, D., Simons, M., & Rosen, P. (2005). Three-dimensional de-  
548 formation caused by the Bam, Iran, earthquake and the origin of shallow slip  
549 deficit. *Nature*, 435(7040), 295–299. doi: 10.1038/nature03425
- 550 Gabriel, A., Ulrich, T., Marchandon, M., Biemiller, J., & Rekoske, J. (2023, 12). 3D  
551 Dynamic Rupture Modeling of the 6 February 2023, Kahramanmaraş, Turkey  
552 Mw 7.8 and 7.7 Earthquake Doublet Using Early Observations. *The Seismic  
553 Record*, 3(4), 342-356. doi: 10.1785/0320230028
- 554 Gabriel, A.-A., Ampuero, J.-P., Dalguer, L. A., & Mai, P. M. (2012). The tran-  
555 sition of dynamic rupture styles in elastic media under velocity-weakening  
556 friction. *Journal of Geophysical Research: Solid Earth*, 117(B9). doi:  
557 10.1029/2012JB009468
- 558 Gao, Z., Li, Y., Shan, X., & Zhu, C. (2021). Earthquake Magnitude Estimation from  
559 High-Rate GNSS Data: A Case Study of the 2021 Mw 7.3 Maduo Earthquake.  
560 *Remote Sensing*, 13(21). doi: 10.3390/rs13214478
- 561 Guo, R., Yang, H., Li, Y., Zheng, Y., & Zhang, L. (2021). Complex Slip Distribution  
562 of the 2021 Mw 7.4 Maduo, China, Earthquake: An Event Occurring on the  
563 Slowly Slipping Fault. *Seismological Research Letters*, 93(2A), 653-665. doi:  
564 10.1785/0220210226
- 565 Harris, R. A., Barall, M., Aagaard, B., Ma, S., Roten, D., Olsen, K., ... Dalguer,  
566 L. (2018, 04). A Suite of Exercises for Verifying Dynamic Earthquake  
567 Rupture Codes. *Seismological Research Letters*, 89(3), 1146-1162. doi:  
568 10.1785/0220170222

- 569 He, K., Wen, Y., Xu, C., & Zhao, Y. (2021, 10). Fault Geometry and Slip Distri-  
570 bution of the 2021 Mw 7.4 Maduo, China, Earthquake Inferred from InSAR  
571 Measurements and Relocated Aftershocks. *Seismological Research Letters*,  
572 *93*(1), 8-20. doi: 10.1785/0220210204
- 573 He, L., Feng, G., Wu, X., Lu, H., Xu, W., Wang, Y., ... Li, Z. (2021). Coseismic  
574 and Early Postseismic Slip Models of the 2021 Mw 7.4 Maduo Earthquake  
575 (Western China) Estimated by Space-Based Geodetic Data. *Geophysical Re-*  
576 *search Letters*, *48*(24), e2021GL095860. (e2021GL095860 2021GL095860) doi:  
577 10.1029/2021GL095860
- 578 Heinecke, A., Breuer, A., Rettenberger, S., Bader, M., Gabriel, A.-A., Pelties, C.,  
579 ... Dubey, P. (2014). Petascale high order dynamic rupture earthquake  
580 simulations on heterogeneous supercomputers. In *Sc '14: Proceedings of the*  
581 *international conference for high performance computing, networking, storage*  
582 *and analysis* (p. 3-14). doi: 10.1109/SC.2014.6
- 583 Hu, F., Oglesby, D. D., & Chen, X. (2021). The effect of depth-dependent stress  
584 in controlling free-surface-induced supershear rupture on strike-slip faults.  
585 *Journal of Geophysical Research: Solid Earth*, *126*(5), e2020JB021459.  
586 (e2020JB021459 2020JB021459) doi: 10.1029/2020JB021459
- 587 Hu, F., Xu, J., Zhang, Z., & Chen, X. (2016). Supershear transition mechanism  
588 induced by step over geometry. *Journal of Geophysical Research: Solid Earth*,  
589 *121*(12), 8738-8749. doi: 10.1002/2016JB013333
- 590 Huang, L., Zhang, B., & Shi, Y. (2021). Stress Transfer at the Northeastern End  
591 of the Bayan Har Block and Its Implications for Seismic Hazards: Insights  
592 From Numerical Simulations. *Earth and Space Science*, *8*(12), e2021EA001947.  
593 (e2021EA001947 2021EA001947) doi: 10.1029/2021EA001947
- 594 Huang, Y., Ampuero, J.-P., & Helmberger, D. V. (2014). Earthquake ruptures  
595 modulated by waves in damaged fault zones. *Journal of Geophysical Research:*  
596 *Solid Earth*, *119*(4), 3133–3154.
- 597 Jara, J., Bruhat, L., Thomas, M. Y., Antoine, S. L., Okubo, K., Rougier, E., ...  
598 Bhat, H. S. (2021). Signature of transition to supershear rupture speed in  
599 the coseismic off-fault damage zone. *Proc Math Phys Eng Sci*, *477*(2255),  
600 20210364. doi: 10.1098/rspa.2021.0364
- 601 Jia, Z., Jin, Z., Marchandon, M., Ulrich, T., Gabriel, A.-A., Fan, W., ... Fialko, Y.  
602 (2023). The complex dynamics of the 2023 Kahramanmaraş, Turkey, Mw 7.8-  
603 7.7 earthquake doublet. *Science*, *0*, eadi0685. doi: 10.1126/science.adi0685
- 604 Jin, Z., & Fialko, Y. (2021). Coseismic and early postseismic deformation due  
605 to the 2021 M7.4 Maduo (China) earthquake. *Geophysical Research Let-*  
606 *ters*, *48*(21), e2021GL095213. (e2021GL095213 2021GL095213) doi:  
607 10.1029/2021GL095213
- 608 Jin, Z., Fialko, Y., Yang, H., & Li, Y. (2023). Transient deformation excited by the  
609 2021 M7.4 Maduo (China) earthquake: Evidence of a deep shear zone. *Journal*  
610 *of Geophysical Research: Solid Earth*, *128*(8), e2023JB026643. (e2023JB026643  
611 2023JB026643) doi: 10.1029/2023JB026643
- 612 Kaneko, Y., & Lapusta, N. (2010). Supershear transition due to a free surface in  
613 3-D simulations of spontaneous dynamic rupture on vertical strike-slip faults.  
614 *Tectonophysics*, *493*(3), 272-284. (Earthquake supershear rupture speeds) doi:  
615 10.1016/j.tecto.2010.06.015
- 616 Käser, M., & Dumbser, M. (2006, 08). An arbitrary high-order discontinuous  
617 Galerkin method for elastic waves on unstructured meshes — I. The two-  
618 dimensional isotropic case with external source terms. *Geophysical Journal*  
619 *International*, *166*(2), 855-877. doi: 10.1111/j.1365-246X.2006.03051.x
- 620 Li, C., Li, T., Hollingsworth, J., Zhang, Y., Qian, L., & Shan, X. (2023). Strain  
621 threshold for the formation of coseismic surface rupture. *Geophysical Research*  
622 *Letters*, *50*(16), e2023GL103666.
- 623 Li, C., Li, T., Shan, X., & Zhang, G. (2023). Extremely Large Off-Fault Deforma-



- tion during the 2021 M w 7.4 Maduo, Tibetan Plateau, Earthquake. *Seismological Society of America*, *94*(1), 39–51.
- Li, Q., Wan, Y., Li, C., Tang, H., Tan, K., & Wang, D. (2022, 03). Source Process Featuring Asymmetric Rupture Velocities of the 2021 Mw 7.4 Maduo, China, Earthquake from Teleseismic and Geodetic Data. *Seismological Research Letters*, *93*(3), 1429-1439. doi: 10.1785/0220210300
- Liu-Zeng, J., Liu, Z., Liu, X., Milliner, C., Rodriguez Padilla, A. M., Xu, S., ... Shao, Z. (2024). Fault orientation trumps fault maturity in controlling coseismic rupture characteristics of the 2021 maduo earthquake [Journal Article]. *AGU Advances*, *5*(2), e2023AV001134. doi: 10.1029/2023AV001134
- Lyu, M., Chen, K., Xue, C., Zang, N., Zhang, W., & Wei, G. (2022). Overall sub-shear but locally supershear rupture of the 2021 Mw 7.4 Maduo earthquake from high-rate GNSS waveforms and three-dimensional InSAR deformation. *Tectonophysics*, *839*, 229542. doi: 10.1016/j.tecto.2022.229542
- Manighetti, I., Caulet, C., Barros, L. D., Perrin, C., Cappa, F., & Gaudemer, Y. (2015). Generic along-strike segmentation of Afar normal faults, East Africa: Implications on fault growth and stress heterogeneity on seismogenic fault planes. *Geochemistry, Geophysics, Geosystems*, *16*, 443-467. doi: 10.1002/2014GC005691
- Milliner, C. W. D., Dolan, J. F., Hollingsworth, J., Leprince, S., Ayoub, F., & Sammis, C. G. (2015). Quantifying near-field and off-fault deformation patterns of the 1992 Mw 7.3 Landers earthquake. *Geochemistry, Geophysics, Geosystems*, *16*(5), 1577-1598. doi: 10.1002/2014GC005693
- Nevitt, J. M., Brooks, B. A., Catchings, R. D., Goldman, M. R., Ericksen, T. L., & Glennie, C. L. (2020). Mechanics of near-field deformation during co-and post-seismic shallow fault slip. *Scientific Reports*, *10*(1), 5031.
- Pan, J., Li, H., Chevalier, M.-L., Tapponnier, P., Bai, M., Li, C., ... Chen, P. (2022). Co-seismic rupture of the 2021, Mw7.4 Maduo earthquake (northern Tibet): Short-cutting of the Kunlun fault big bend. *Earth and Planetary Science Letters*, *594*, 117703. doi: 10.1016/j.epsl.2022.117703
- Pelties, C., Gabriel, A.-A., & Ampuero, J.-P. (2014). Verification of an ADER-DG method for complex dynamic rupture problems. *Geoscientific Model Development*, *7*(3), 847–866. doi: 10.5194/gmd-7-847-2014
- Perrin, C., Manighetti, I., & Gaudemer, Y. (2016). Off-fault tip splay networks: A genetic and generic property of faults indicative of their long-term propagation. *Comptes Rendus Geoscience*, *348*(1), 52–60.
- Ramos, M. D., Thakur, P., Huang, Y., Harris, R. A., & Ryan, K. J. (2022). Working with Dynamic Earthquake Rupture Models: A Practical Guide. *Seismological Research Letters*, *93*(4), 2096-2110. doi: 10.1785/0220220022
- Ren, J., Zhang, Z., Gai, H., & Kang, W. (2021). Typical Riedel shear structures of the coseismic surface rupture zone produced by the 2021 Mw 7.3 Maduo earthquake, Qinghai, China, and the implications for seismic hazards in the block interior. *Natural Hazards Research*, *1*(4), 145-152. doi: 10.1016/j.nhres.2021.10.001
- Rodriguez Padilla, A. M., & Oskin, M. E. (2023). Displacement Hazard from Distributed Ruptures in Strike-Slip Earthquakes. *Bulletin of the Seismological Society of America*, *113*(6), 2730-2745. doi: 10.1785/0120230044
- Roten, D., Olsen, K. B., Day, S. M., Cui, Y., & Fäh, D. (2014). Expected seismic shaking in Los Angeles reduced by San Andreas fault zone plasticity. *Geophysical Research Letters*, *41*(8), 2769-2777. doi: 10.1002/2014GL059411
- Scott, C. P., Arrowsmith, J. R., Nissen, E., Lajoie, L., Maruyama, T., & Chiba, T. (2018). The M7 2016 Kumamoto, Japan, earthquake: 3-D deformation along the fault and within the damage zone constrained from differential lidar topography. *Journal of Geophysical Research: Solid Earth*, *123*(7), 6138–6155.
- Styron, R., Taylor, M., & Okoronkwo, K. (2010). Database of Active Structures

- 679 From the Indo-Asian Collision. *Eos, Transactions American Geophysical*  
680 *Union*, 91(20), 181-182. doi: 10.1029/2010EO200001
- 681 Tang, R., Yuan, J., & Gan, L. (2021). Free-surface-induced supershear transition in  
682 3-d simulations of spontaneous dynamic rupture on oblique faults. *Geophysical*  
683 *Research Letters*, 48(3), e2020GL091621. (e2020GL091621 2020GL091621) doi:  
684 10.1029/2020GL091621
- 685 Taufiqurrahman, T., Gabriel, A.-A., Li, D., Ulrich, T., Li, B., Carena, S., ...  
686 Gallovič, F. (2023, Jun 01). Dynamics, interactions and delays of the  
687 2019 Ridgecrest rupture sequence. *Nature*, 618(7964), 308-315. doi:  
688 10.1038/s41586-023-05985-x
- 689 Templeton, E. L., & Rice, J. R. (2008). Off-fault plasticity and earthquake rup-  
690 ture dynamics: 1. Dry materials or neglect of fluid pressure changes. *Journal of*  
691 *Geophysical Research: Solid Earth*, 113(B09306). doi: 10.1029/2007JB005529
- 692 Tinti, E., Casarotti, E., Ulrich, T., Taufiqurrahman, T., Li, D., & Gabriel, A.-A.  
693 (2021). Constraining families of dynamic models using geological, geodetic  
694 and strong ground motion data: The Mw 6.5, October 30th, 2016, Norcia  
695 earthquake, Italy. *Earth and Planetary Science Letters*, 576, 117237. doi:  
696 10.1016/j.epsl.2021.117237
- 697 Ulrich, T., Gabriel, A.-A., Ampuero, J.-P., & Xu, W. (2019). Dynamic viability of  
698 the 2016 Mw 7.8 Kaikōura earthquake cascade on weak crustal faults. *Nature*  
699 *communications*, 10(1), 1213. doi: 10.1038/s41467-019-09125-w
- 700 UNICEF China. (2021, Jun). *UNICEF Sends Supplies to Children Affected by an*  
701 *Earthquake in Qinghai Province*. Retrieved from [https://www.unicef.cn/en/](https://www.unicef.cn/en/press-releases/unicef-sends-supplies-children-affected-earthquake-qinghai-province)  
702 [press-releases/unicef-sends-supplies-children-affected-earthquake](https://www.unicef.cn/en/press-releases/unicef-sends-supplies-children-affected-earthquake-qinghai-province)  
703 [-qinghai-province](https://www.unicef.cn/en/press-releases/unicef-sends-supplies-children-affected-earthquake-qinghai-province)
- 704 Uphoff, C., Rettenberger, S., Bader, M., Madden, E. H., Ulrich, T., Wollherr, S.,  
705 & Gabriel, A.-A. (2017). Extreme scale multi-physics simulations of the  
706 tsunamigenic 2004 sumatra megathrust earthquake. In *Proceedings of the in-*  
707 *ternational conference for high performance computing, networking, storage*  
708 *and analysis*. New York, NY, USA: Association for Computing Machinery. doi:  
709 10.1145/3126908.3126948
- 710 USGS. (2021). *Overview: M7.3 - Southern Qinghai, China*. Retrieved from  
711 [https://earthquake.usgs.gov/earthquakes/eventpage/us7000e54r/](https://earthquake.usgs.gov/earthquakes/eventpage/us7000e54r/executive)  
712 [executive](https://earthquake.usgs.gov/earthquakes/eventpage/us7000e54r/executive)
- 713 Wang, M., Wang, F., Jiang, X., Tian, J., Li, Y., Sun, J., & Shen, Z.-K. (2021, 11).  
714 GPS determined coseismic slip of the 2021 Mw 7.4 Maduo, China, earthquake  
715 and its tectonic implication. *Geophysical Journal International*, 228(3), 2048-  
716 2055. doi: 10.1093/gji/ggab460
- 717 Wang, S., Song, C., Li, S., & Li, X. (2022). Resolving co-and early post-seismic slip  
718 variations of the 2021 Mw 7.4 Madoi earthquake in east Bayan Har block with  
719 a block-wide distributed deformation mode from satellite synthetic aperture  
720 radar data. *Earth Planet. Phys*, 6(1), 108–122. doi: 10.26464/epp2022007
- 721 Wang, W., Fang, L., Wu, J., Tu, H., Chen, L., Lai, G., & Zhang, L. (2021).  
722 Aftershock sequence relocation of the 2021 Ms 7.4 Maduo earthquake,  
723 Qinghai, China. *Science China Earth Sciences*, 64, 1371–1380. doi:  
724 10.1007/s11430-021-9803-3
- 725 Wei, S., Zeng, H., Shi, Q., Liu, J., Luo, H., Hu, W., ... Wang, T. (2022). Simul-  
726 taneous rupture propagation through fault bifurcation of the 2021 Mw 7.4  
727 Maduo earthquake. *Geophysical Research Letters*, 49(21), e2022GL100283.  
728 (e2022GL100283 2022GL100283) doi: 10.1029/2022GL100283
- 729 Wen, Y., Cai, J., He, K., & Xu, C. (2024). Dynamic Rupture of the 2021 MW 7.4  
730 Maduo Earthquake: An Intra-Block Event Controlled by Fault Geometry. *J.*  
731 *Geophys. Res.*, 129(1), e2023JB027247. doi: 10.1029/2023JB027247
- 732 Wollherr, S., Gabriel, A.-A., & Mai, P. M. (2019). Landers 1992 “reloaded”: In-  
733 tegrative dynamic earthquake rupture modeling. *Journal of Geophysical Re-*

- 734 search: *Solid Earth*, 124(7), 6666-6702. doi: 10.1029/2018JB016355
- 735 Wollherr, S., Gabriel, A.-A., & Uphoff, C. (2018). Off-fault plasticity in three-
- 736 dimensional dynamic rupture simulations using a modal Discontinuous
- 737 Galerkin method on unstructured meshes: Implementation, verification and
- 738 application. *Geophysical Journal International*, 214(3), 1556–1584. doi:
- 739 10.1093/GJI/GGY213
- 740 Xin, H., Zhang, H., Kang, M., He, R., Gao, L., & Gao, J. (2018, 10). High-
- 741 Resolution Lithospheric Velocity Structure of Continental China by Double-
- 742 Difference Seismic Travel-Time Tomography. *Seismological Research Letters*,
- 743 90(1), 229-241. doi: 10.1785/0220180209
- 744 Xu, B., & Zhang, Y. (2023). Joint inversion of centroid moment tensor for large
- 745 earthquakes by combining teleseismic P-wave and W-phase records. *Geophysi-*
- 746 *cal Journal International*, 234(2), 1143-1156. doi: 10.1093/gji/ggad128
- 747 Xu, J., Zhang, H., & Chen, X. (2015, 07). Rupture phase diagrams for a planar fault
- 748 in 3-D full-space and half-space. *Geophysical Journal International*, 202(3),
- 749 2194-2206. doi: 10.1093/gji/ggv284
- 750 Yuan, J., & Li, Y. (2023). Complex fault geometry controls dynamic rupture of
- 751 the 2021 Mw7.4 Maduo earthquake, NE Tibetan Plateau. *Tectonophysics*, 868,
- 752 230105. doi: <https://doi.org/10.1016/j.tecto.2023.230105>
- 753 Yuan, Z., Li, T., Su, P., Sun, H., Ha, G., Guo, P., . . . Thompson Jobe, J. (2022).
- 754 Large Surface-Rupture Gaps and Low Surface Fault Slip of the 2021 Mw 7.4
- 755 Maduo Earthquake Along a Low-Activity Strike-Slip Fault, Tibetan Plateau.
- 756 *Geophysical Research Letters*, 49(6), e2021GL096874. (e2021GL096874
- 757 2021GL096874) doi: 10.1029/2021GL096874
- 758 Yue, H., Shen, Z.-K., Zhao, Z., Wang, T., Cao, B., Li, Z., . . . Xue, L. (2022).
- 759 Rupture process of the 2021 M7.4 Maduo earthquake and implication for
- 760 deformation mode of the Songpan-Ganzi terrane in Tibetan Plateau. *Pro-*
- 761 *ceedings of the National Academy of Sciences*, 119(23), e2116445119. doi:
- 762 10.1073/pnas.2116445119
- 763 Zhang, P., Deng, Q., Zhang, G., Ma, J., Gan, W., Min, W., . . . Wang, Q. (2003,
- 764 Feb 01). Active tectonic blocks and strong earthquakes in the continent
- 765 of China. *Science in China Series D: Earth Sciences*, 46(2), 13-24. doi:
- 766 10.1360/03dz0002
- 767 Zhang, X., Feng, W., Du, H., Samsonov, S., & Yi, L. (2022). Supershear rupture
- 768 during the 2021 Mw 7.4 Maduo, China, earthquake. *Geophysical Research Let-*
- 769 *ters*, 49(6), e2022GL097984. (e2022GL097984 2022GL097984) doi: 10.1029/
- 770 2022GL097984
- 771 Zhu, M., Chen, F., Fu, B., Chen, W., Qiao, Y., Shi, P., . . . Gao, S. (2023).
- 772 Earthquake-induced risk assessment of cultural heritage based on InSAR and
- 773 seismic intensity: A case study of Zhalang temple affected by the 2021 Mw 7.4
- 774 Maduo (China) earthquake. *International Journal of Disaster Risk Reduction*,
- 775 84, 103482. doi: 10.1016/j.ijdr.2022.103482
- 776 Zhu, Y., Diao, F., Fu, Y., Liu, C., & Xiong, X. (2021, Aug 01). Slip rate of the
- 777 seismogenic fault of the 2021 Maduo earthquake in western China inferred
- 778 from GPS observations. *Science China Earth Sciences*, 64(8), 1363-1370. doi:
- 779 10.1007/s11430-021-9808-0

# Supporting Information for “Non-typical supershear rupture: fault heterogeneity and segmentation govern unilateral supershear and cascading multi-fault rupture in the 2021 $M_w$ 7.4 Maduo Earthquake”

J. N. Hayek<sup>1</sup>, M. Marchandon<sup>1</sup>, D. Li<sup>1,6</sup>, L. Pousse-Beltran<sup>3</sup>, J.

Hollingsworth<sup>3</sup>, T. Li<sup>4,5</sup>, A.-A. Gabriel<sup>2,1</sup>

<sup>1</sup>Ludwig-Maximilians-Universität Munich, Germany

<sup>2</sup>Scripps Institution of Oceanography, UC San Diego, La Jolla, USA

<sup>3</sup>Université Grenoble Alpes, Université Savoie Mont Blanc, CNRS, IRD, Univ. Gustave Eiffel, ISTerre, 38000 Grenoble, France

<sup>4</sup>State Key Laboratory of Earthquake Dynamics, Institute of Geology, China Earthquake Administration, Beijing, China

<sup>5</sup>Xinjiang Pamir Intracontinental Subduction National Observation and Research Station, Beijing, China

<sup>6</sup>GNS Science, Lower Hutt, New Zealand

## Contents of this file

1. Text S1 to S6
2. Figures S1 to S26
3. Table S1
4. Movie S1

The supplementary material contains a detailed description of our dynamic rupture model and the initial stress setup (Text S1), the method used for our geodetic analysis (geodetic inversion and fault zone width estimation, Text S2), the method used for

---

the analysis of the modeled off-fault plasticity patterns (Text S3) and sensitivity analysis based on 8 alternative dynamic rupture models, including two alternative dynamic rupture scenarios with homogeneous characteristic slip distance  $D_{RS}$ , two scenarios with alternative plastic cohesion (Text S4), two models with different fault geometries (Text S5) and two models with different initial stresses (Text S6).

## **Text S1: Dynamic rupture mesh generation and model setup**

### **Mesh generation**

We include our geodetically inferred fault system and the topographic data of 1-arc-minute resolution from ETOPO1 (Amante & Eakins, 2009) in the model domain. The topographic surface is discretized into triangles of  $\sim 2$  km in length. We set the edge lengths of elements in the vicinity of the fault interface to 200 m as an upper limit, ensuring adequate resolution in space and time. We generate the tetrahedral elements in a cubic domain using SimModeler (Simmetrix Inc., 2017), with an increased refinement of the element size towards the fault to ensure computational accuracy and efficiency. The mesh is gradually coarsened based on the distance normal to the fault surface at a gradient of 0.3, gradually reducing the resolution for outgoing seismic waves to improve simulation efficiency.

We assign the boundary conditions as free surface, dynamic rupture, and absorbing boundary to the topographic surface, the fault surfaces, and the domain lateral and bottom surfaces, respectively. We set the entire domain size to  $590 \text{ km} \times 488 \text{ km} \times 96 \text{ km}$ , large enough to avoid any waves reflecting at the imperfectly absorbing boundaries at the lateral and bottom domain boundaries to pollute our simulation results. The computational mesh consists of 5,958,234 elements in total. A simulation with 4th-order accuracy in time and space for 90 s requires  $\approx 2,800$  CPU hours on the supercomputer SuperMUC-NG at

the Leibniz supercomputing center in Garching.

The size of the area behind the rupture front in which shear stress decreases from its static to its dynamic value is the process zone width (Day et al., 2005). The on-fault resolution (mesh size and order of accuracy) must be chosen to be high enough to resolve the process zone and ensure an adequate numerical resolution of rupture dynamics. In our preferred dynamic rupture model the *minimum* process zone width averaged across the 5% of the fault elements with the smallest process zone sizes during rupture is 232 m. Our on-fault element size is  $h = 200$  m, noting that each dynamic rupture element provides sub-element resolution.

### Initial background stresses of the preferred dynamic rupture model

In this section, we detail the initial stress parametrization, summarized in section 2.2 of the main text. We assume an ambient homogeneous background stress acting within the model domain. (Taufiqurrahman et al., 2023) In addition, all faults include heterogeneous initial stresses as inferred from the geodetically-constrained fault slip (Jia et al., 2023).

We set a homogeneous background stress according to a virtual fault plane derived from regional focal mechanism inversions (USGS, 2021), as described in Table S1. The absolute values of confining stresses are jointly defined by the lithostatic loading  $\sigma_z$ , the ratio of pore fluid pressure  $\lambda$ , the relative fault strength  $R_0$ , the stress shape ratio  $\nu$ , and a depth-dependent shape function  $\Omega(z)$  (Ulrich et al., 2019).

The lithostatic stress increases linearly with depth below the topographic surface. The lithostatic pressure  $\sigma_z$  at depth  $z$  follows:

$$\sigma_z = \int_0^z \rho(z_i) g z_i \partial z_i \quad (1)$$

In nature, the temperature-dependent brittle-ductile transition is expected to reduce the deviatoric stress at the base of the seismogenic zone, reflecting the yield strength variation of the lithosphere (e.g., Scholz, 1988). Here, we use a stress modulation function  $\Omega_z$ , defined as varying with depth and smoothly reducing the deviatoric stresses below the seismogenic depth (Ulrich et al., 2019). Figure S3 shows the depth distribution of  $\Omega_z$  used in the reference model.

Our depth-dependent effective normal stress is accounting for pore fluid pressure (Madden et al., 2022). We assume that the fluid pressure throughout the crust is proportional to the lithostatic stress, expressed as  $P_f = \gamma\sigma_c$  with  $\gamma$  being the fluid-pressure ratio defined by  $\frac{\rho_{water}}{\rho_{rock}}$ . The effective confining stress is defined as  $\sigma_c = (1 - \gamma)\sigma_z$ . We assume in our model a hydrostatic stress state, implying  $(1 - \gamma) = 0.63$ .

The fault prestress ratio  $R_0$  describes the closeness to failure of an optimally oriented virtual plane according to Mohr-Coulomb theory (Aochi & Madariaga, 2003). We assume a uniform distribution of prestress ratio  $R_0$ . The stress shape ratio  $\nu$ , which is defined as  $\frac{S_2 - S_3}{S_1 - S_3}$ , balances the principal stresses ( $S_1$ ,  $S_2$ , and  $S_3$ ; ordered from most compressional to most tensional). We assume  $\nu = 0.5$  for the entire fault.

### **Initial heterogeneous stresses inferred from geodetically-constrained fault slip**

We use the geodetic static slip model as input in a dynamic relaxation simulation with SeisSol (Tinti et al., 2021; Jia et al., 2023) using the same computational mesh, fault geometries, and subsurface material parameters to compute the corresponding shear and normal stress changes. The resulting stress changes are scaled by a factor of 0.3 and then added to the ambient, regional initial shear, and normal on-fault prestress amplitudes.

This balance is constrained by a few trial-and-error dynamic rupture simulations, ensuring realistic slip distributions and moment rate release.

The included stress variation inferred from our geodetically-inferred slip distribution (Supplementary Text S2) further constrains the initial on-fault stress conditions. We use SeisSol to compute the total stress perturbations associated with the imposed kinematic slip on the fault surface as a boundary condition, ensuring the same spatial discretization. The six components of the stress tensor in each volumetric element are added to the background stresses which have been introduced above. This operation results in a heterogeneous initial shear and normal stresses on the fault (Figure S1).

### **3D dynamic rupture model setup details**

We perform all 3D dynamic rupture and seismic wave propagation models using the open-source package SeisSol ([www.seissol.org](http://www.seissol.org)), which is based on the Arbitrary High-order Derivative Discontinuous Galerkin finite element method (Käser & Dumbser, 2006; Dumbser & Käser, 2006; Pelties et al., 2012), and is optimized for modern high-performance computing architectures including an efficient local time-stepping algorithm (Breuer et al., 2014; Heinecke et al., 2014; Uphoff et al., 2017; Krenz et al., 2021). Dynamic rupture simulations using SeisSol have been validated against several community benchmarks following the SCEC/USGS Dynamic Rupture Code Verification exercises (Pelties et al., 2014; Harris et al., 2018).

Within the off-fault plasticity implementation (Wollherr et al., 2018), the onset of Drucker-Prager plastic yielding is not instantaneous but governed by rate-dependent viscoplastic relaxation with a relaxation time  $T_v$  of 0.05 s, which ensures convergence of simulation results with mesh refinement (Wollherr et al., 2018).

### **Nucleation**



We initiate the spontaneous dynamic rupture by imposing an over-stressed spherical patch with a radius of 950 m centered at the USGS hypocentral location ( $34.61^\circ$ ,  $98.36^\circ$ ), at a depth of 5.5 km. The stress loading gradually increases exponentially over the first 0.5 s to achieve smoothly expanding rupture, following the best practices established in the community verification benchmark project of the USGS and SCEC (Harris et al., 2009, 2018).

## **Text S2: Geodetic data processing, static inversion and surface deformation analysis**

In this section, we describe the processing of the Sentinel-1 SAR and Sentinel-2 and SPOT6/7 optical data, the method used to estimate the fault slip distribution from the joint inversion of InSAR and Sentinel-2 optical data, and the method used to characterize the off-fault deformation from high-resolution SPOT6/7 optical data.

### **InSAR processing**

We processed two six-day interferograms using ascending and descending SAR images from the Sentinel-1 constellation operated by the European Space Agency. The pre- and post-earthquake SAR images were acquired on the 20th May 2021 and 26th May 2021, respectively, by the ascending track A099 and descending track D106. We processed the interferograms using the NSBAS processing chain (New Small BAseline Subset Doin et al., 2011; Thollard et al., 2021). The topographic phase contribution has been removed from the interferograms using the Shuttle Radar Topography Mission (SRTM; Farr et al., 2007) 3 arc-sec ( $\approx 90$  m resolution) Digital Elevation Model (DEM). Finally, the interferograms were filtered using a coherence-dependent filter and unwrapped using the branch-cut algorithm of Doin et al. (2015) and Grandin et al. (2012).

## Optical data processing

We measured a medium-resolution (40 m grid spacing) and a high-resolution (6 m grid spacing) horizontal displacement field for the Maduo earthquake from the correlation of Sentinel-2 and SPOT6/7 images, respectively.

For the medium resolution displacement field, we used three pairs of pre- and post-earthquake Sentinel-2 optical images acquired on 4th August 2017 and 19th July 2021, respectively. The pre- and post-earthquake image dates have been chosen to minimize illumination bias in the resulting correlation. We correlate the images using the phase correlator of the open-source software package COSI-Corr (Leprince et al., 2007) using a multiscale sliding correlation window of 128 to 32 pixels and a measurement step of 4 pixels (40 m). Data points with Signal-over-Noise Ratio (SNR) lower than 0.9 and unrealistic displacement amplitudes were discarded. Outliers were also removed using a neighborhood statistical approach, whereby values are masked if  $< 50\%$  of neighbors within a 18-by-18 pixel window centered on each pixel lie within a threshold value from the central pixel value (Zinke et al., 2019). Finally, the correlation maps have been smoothed with a 3-by-3 median filter. The three image pairs were processed independently, then overlapping correlation scenes were aligned by removing a residual ramp over each correlation.

We measure the a high resolution horizontal surface displacement field for the Maduo earthquake from the correlation of SPOT-6/7 images of 1.5 m resolution. Six pairs of pre- and post-earthquake images are needed to cover the entire rupture.

In order to obtain a seamless displacement field, the pre- and post- SPOT images are first registered to pre- and post 10 m resolution Sentinel-2 images used as reference. For this registration step, using the Ames Stereo Pipeline (ASP) software, we first correlated the pre/post Sentinel-2 reference images with the raw pre/post SPOT images. We transform the correlation maps obtained into Ground Control Points (GCPs), which are then used

to refine the Rational Polynomial Coefficients (RPCs) of the SPOT images. The pre- and post-earthquake raw SPOT images are then orthorectified with the same pre-earthquake WorldDEM of 2.5 m resolution.

We use the phase correlator of COSI-Corr to correlate the orthorectified pre- and post-orthoimages. We used a multi-scale correlation windows of 128-to-32 pixels and a step size of 4 pixels, leading to a final spatial resolution of 6 m. Because we use a step size smaller than the correlation window, the measurements are truly independent every 8 pixels (24 m), since the correlation process gives a single displacement value per sub-pixel refinement window (which is approx. half of 32 pixels in this case, when we account for the windowing function used to mitigate spectral leakage when computing the FFT of the pre/post image windows).

As we orthorectified the pre- and post-images using the same pre-earthquake DEM, the raw optical displacement correlation maps contain a strong stereoscopic noise component in addition to the coseismic displacement signal. To denoise the correlation maps, we trained a random forest algorithm to predict the stereoscopic bias from the local slope, local aspect, local height, and local grayscale pixel values of the pre- and post-earthquakes images. This bias is learned away from the fault, using flattened (i.e. detrended) displacement data. The predicted bias over the entire fault zone is then removed from the displacement maps.

Finally, outliers are removed using the neighborhood statistical approach, along with data points with a low SNR ratio ( $< 0.9$ ), and unrealistic amplitudes. TV-L1 smoothing is then applied to the displacement map to further reduce high-frequency noise, while preserving sharp features associated with the surface ruptures.

## Data subsampling

In order to reduce the computation time of the inversion, we downsampled the Sentinel-1 InSAR and Sentinel-2 optical displacement data using a subsampling scheme that depends on the distance perpendicular to the fault (Grandin et al., 2009). For distances lower than 17 km from the fault, we downsampled the interferograms to one point every 2 km. For distances between 17 and 30 km from the fault, we kept one point every 4 km, for distances between 30 and 45 km from the fault, we kept one point every 8 km, and for distances greater than 45 km, we kept one point every 16 km. The Sentinel-2 optical data cover only the near- and medium-field (up to 40 km from the fault) and are downsampled to one point every 2 km.

## Static fault slip model from joint inversion of InSAR and Sentinel-2 optical data

We infer the fault slip distribution at depth for the Maduo earthquake from the joint inversion of the subsampled Sentinel-1 InSAR and Sentinel-2 optical data. We used the same segmented fault geometry as the one used in our dynamic rupture model (see Method section and SI Text S1) that we discretized with triangular subfaults of variable size. The subfault size increases gradually with depth from 1 km at the surface to 5 km at 20 km depth. We computed the Green's functions relating a unit of slip on the subfaults to the surface displacements assuming a uniform elastic half-space with a Poisson ratio  $\nu$  of 0.25 (Meade et al. 2007). We solved for the strike and dip component of the slip on each subfault using a constrained linear least square inversion (Coleman & Li, 1992). We constrained the strike-slip between 0 and 10 m, the dip-slip between -10 and 10 m and we implement a Laplacian smoothing operator to avoid large slip variations between neighboring patches. We are therefore solving the following system of equations:

$$\begin{bmatrix} \mathbf{d} \\ 0 \end{bmatrix} = \begin{bmatrix} \mathbf{G} \\ \lambda \mathbf{D} \end{bmatrix} \mathbf{m} \quad (2)$$

where  $\mathbf{d}$  is the data vector composed of the subsampled InSAR and optical data;  $\mathbf{G}$  is the Green's functions matrix relating a unit slip on each subfault to the surface displacements,  $\mathbf{m}$  is the vector of parameters we are solving for (strike-slip and dip-slip on each subfaults),  $D$  is the second-order finite difference operator and  $\lambda$  is the smoothing factor that we choose according to an L-curve criterion (Figure S5). In addition to the strike- and dip-slip on the fault, we also solved for residual ramps in the InSAR and optical data. We weighted the data such that the InSAR and optical datasets are equally well fit. Figures S6 and S7 show that the data are well reproduced by our model, with an RMS misfit of 0.03 m and 0.031 m for the ascending and descending interferograms, and 0.20 m and 0.15 m for the EW and NS optical displacement fields, respectively.

### **Fault zone width estimation from the SPOT6/7 displacement field**

To estimate the amount of surface slip accommodated across the fault zone as well as the fault zone width, we measure 509 fault-perpendicular stacked profiles spaced every 300 m along the fault trace. Each profile is  $\sim 10$  km long and corresponds to the stack of 50 parallel profiles measured over a width of 300 m. This choice of stack width represents the optimal trade-off maximizing the signal-over-noise ratio while preserving spatial resolution along-strike. For each profile, we fit linear regressions to the displacement profile on each side of the fault from the far-field to the inflection point near the fault trace (see Figure S25). The fault offset is then measured by computing the displacement difference of the linear regressions where they project to the fault trace, while the fault zone width corresponds to the distance between the inflection points on both sides of the fault.

### **Text S3: Surface sampling of the modelled off-fault plasticity**

The accumulated 3D plastic strain field can be mapped into a scalar quantity following (Ma, 2008; Wollherr et al., 2019). We sample the modeled off-fault plasticity at fault-parallel transects (Figure S8), selecting the nearest cell center location to the sampling point using a KDTree algorithm. Subsequently, we organize the scalar values of the modeled accumulated plastic strain for each transect and present a sorted histogram alongside both geodetically derived and simulated fault-parallel offsets (Figure 4B).

**Text S4: Alternative rupture scenarios: sensitivity to on- and off-fault properties**

In this section, we present alternative rupture scenarios to explore the sensitivity of our results to on- and off-fault rheology parameterizations different to the preferred model. Specifically, we explore the effects of prescribing a homogeneous critical slip distance  $D_{RS}$  on all faults and of changing the off-fault plastic cohesion values. In the following, we use our preferred model as a reference to which we compare the dynamic rupture behavior in alternative models.

**Alternative models with homogeneous  $D_{RS}$  on the entire fault**

We present two models with homogeneous  $D_{RS}=0.025$  in Figure S9, and  $D_{RS}=0.125$  in Figure S11. The first homogeneous  $D_{RS}$  model results in sustained bilaterally rupturing supershear propagation, which effectively activates the southeastern fault branches. The second model with larger  $D_{RS}$  results in bilateral subshear propagation, which fails to trigger the southeastern fault branches. This suggests that the conditions under which sustained supershear rupture can form, as well as the supershear propagation itself, effectively facilitate rupture jumping to the southeastern fault branches.

### **Alternative rupture scenarios: sensitivity to off-fault plastic cohesion**

We present two alternative choices for the bulk plastic cohesion  $C_{plast}$ . The first model has a lower value  $C_{plast} = 1e - 4$  and is shown in Figure S14. This model results in a significantly increased accumulated plastic strain compared to the preferred model. Additionally, this model fails to activate the southernmost fault segment. The second model, with a larger value  $C_{plast} = 5e - 4$ , features significantly reduced off-fault plasticity (Figure S16). In this second case, dynamic rupture propagates across all fault segments. The energy dissipated in the damage zone can become a significant fraction of the total fracture energy (Andrews, 2005; Templeton & Rice, 2008; Gabriel et al., 2013), which can, in turn, affect the dynamics of rupture propagation. These models illustrate the sensitive balance of sustained multi-fault rupture and off-fault deformation patterns to strongly or weakly deforming bulk material.

### **Text S5: Alternative rupture scenarios: sensitivity to the fault system geometry**

We highlight the effects of fault geometries, specifically of segmentation and dip angles, while keeping the material, friction, and stress parametrizations unchanged. Figure S17 showcases a scenario in which segments F1 and F2 are connected smoothly and not separated. The fault surface traces are then extruded with a constant dipping angle of  $83^\circ$  towards the North.

In contrast, Figure S19 showcases a scenario in which the segmentation is the same as in our preferred model but the three segments F1, F2, and F3 dip with a constant dipping angle of  $83^\circ$  towards the North.

The first geometrical variation features dynamic rupture continuously propagating with supershear velocity towards the east, with no secondary onset of supershear rupture after

the activation of the second branch as in our preferred model. The modeled moment rate release has a shorter local minimum between the main peaks Figure S17B.

The off-fault plasticity distribution is mainly widespread across the southernmost branch (Figure S18A). This leads to a single large bell-shaped distribution centered at  $99^\circ$  Longitude (Figure S18B), in contrast to three widely distributed regions of off-fault plastic strain, that are associated with the fault geometrical variations of the second segment in the preferred model. The latter better resembles the observed distribution of optical fault zone width (Figure 4B).

The model with different dip angles fails to dynamically trigger the fault segments F2 and F3 (Figure S19A). It does not match the second peak in moment rate release (Figure S19B), nor generate any off-fault plasticity distribution beyond  $98.8^\circ$  Longitude.

### **Text S6: Alternative rupture scenarios: sensitivity to the ambient stress orientation**

We showcase alternative models with different ambient stress choices relative to the initial stress parametrization used in the preferred model. Figure S21 shows model results when assuming a strike of  $100^\circ$  for the virtual plane of optimal stress orientation (compared to  $110^\circ$  in the preferred model). This 10 degree change results in higher accumulated on-fault slip, and a nucleation-induced supershear transition, preferentially sustained eastwards. We note that these changes also relate to the fact that the model required a relative increase of prestress parameter  $R_0$  of 0.25 to induce a successful nucleation that led to a propagating rupture.

The second model (Figure S23) deviates from the preferred model in using an optimal stress orientation at a strike of  $120^\circ$ . Now, the modeled on-fault slip amplitudes are lower. No sustained supershear rupture is induced from the nucleation, which is similarly elevated as in the previous model. However, there is an episode of unsustained supers-



hear propagating eastward, induced by a P-/SV-wave transition at the free surface. The duration of the moment rate release is longer than the preferred model, comparing well with the pattern from the USGS, yet the moment rate release amplitudes are low. Additionally, this model fails to rupture the southernmost fault segment. This model leads to slightly wider off-fault plastic strain in the western section of the fault system compared to the eastern section. While this scenario illustrates that a less-optimal background stress orientation can lead to an episode of unsustained supershear and realistic moment rate release, it fails to reproduce observed slip and seismic moment amplitudes and does not dynamically trigger all fault segments. Also the modeled differences in fault zone widths of the eastern and western segments are not agreeing with observations.

## References

- Amante, C., & Eakins, B. W. (2009). *ETOPO1 Global Relief Model converted to PanMap layer format* [data set]. PANGAEA. Retrieved from <https://doi.org/10.1594/PANGAEA.769615> doi: 10.1594/PANGAEA.769615
- Andrews, D. J. (2005). Rupture dynamics with energy loss outside the slip zone. *Journal of Geophysical Research: Solid Earth*, *110*(B01307). doi: 10.1029/2004JB003191
- Aochi, H., & Madariaga, R. (2003). The 1999 Izmit, Turkey, Earthquake: Nonplanar Fault Structure, Dynamic Rupture Process, and Strong Ground Motion. *Bulletin of the Seismological Society of America*, *93*(3), 1249-1266. doi: 10.1785/0120020167
- Breuer, A., Heinecke, A., Rettenberger, S., Bader, M., Gabriel, A.-A., & Pelties, C. (2014). Sustained petascale performance of seismic simulations with seissol on supermuc. In J. M. Kunkel, T. Ludwig, & H. W. Meuer (Eds.), *Supercomputing* (pp. 1–18). Cham: Springer International Publishing.
- Coleman, T. F., & Li, Y. (1992). A globally and quadratically convergent affine scaling method for linear  $n^2$  problems. *Mathematical Programming*, *56*(1-3), 189–222.

- Day, S. M., Dalguer, L. A., Lapusta, N., & Liu, Y. (2005). Comparison of finite difference and boundary integral solutions to three-dimensional spontaneous rupture. *Journal of Geophysical Research: Solid Earth*, *110*(B12). doi: 10.1029/2005JB003813
- Doin, M.-P., Lodge, F., Guillaso, S., Jolivet, R., Lasserre, C., Ducret, G., ... Pinel, V. (2011). Presentation of the small baselin nsbas processing chain on a case example: The etan deformation monitoring from 2003 to 2010 using envisat data. In *Fringe symposium*.
- Doin, M.-P., Twardzik, C., Ducret, G., Lasserre, C., Guillaso, S., & Jianbao, S. (2015). Insar measurement of the deformation around siling co lake: Inferences on the lower crust viscosity in central tibet. *Journal of Geophysical Research: Solid Earth*, *120*(7), 5290–5310.
- Dumbser, M., & Käser, M. (2006, 10). An arbitrary high-order discontinuous Galerkin method for elastic waves on unstructured meshes — II. The three-dimensional isotropic case. *Geophysical Journal International*, *167*(1), 319-336. doi: 10.1111/j.1365-246X.2006.03120.x
- Farr, T. G., Rosen, P. A., Caro, E., Crippen, R., Duren, R., Hensley, S., ... others (2007). The shuttle radar topography mission. *Reviews of geophysics*, *45*(2).
- Gabriel, A.-A., Ampuero, J.-P., Dalguer, L. A., & Mai, P. M. (2013). Source properties of dynamic rupture pulses with off-fault plasticity. *Journal of Geophysical Research: Solid Earth*, *118*(8), 4117-4126. doi: 10.1002/jgrb.50213
- Grandin, R., Doin, M.-P., Bollinger, L., Pinel-Puysségur, B., Ducret, G., Jolivet, R., & Sapkota, S. N. (2012). Long-term growth of the himalaya inferred from interseismic insar measurement. *Geology*, *40*(12), 1059–1062.
- Grandin, R., Socquet, A., Binet, R., Klinger, Y., Jacques, E., De Chabalier, J.-B., ... others (2009). September 2005 manda hararo-dabbahu rifting event, afar (ethiopia):

constraints provided by geodetic data. *Journal of Geophysical Research: Solid Earth*, *114*(B8).

Harris, R. A., Barall, M., Aagaard, B., Ma, S., Roten, D., Olsen, K., ... Dalguer, L. (2018, 04). A Suite of Exercises for Verifying Dynamic Earthquake Rupture Codes. *Seismological Research Letters*, *89*(3), 1146-1162. doi: 10.1785/0220170222

Harris, R. A., Barall, M., Archuleta, R., Dunham, E., Aagaard, B., Ampuero, J. P., ... Templeton, E. (2009). The SCEC/USGS Dynamic Earthquake Rupture Code Verification Exercise. *Seismological Research Letters*, *80*(1), 119-126. doi: 10.1785/gssrl.80.1.119

Heinecke, A., Breuer, A., Rettenberger, S., Bader, M., Gabriel, A.-A., Pelties, C., ... Dubey, P. (2014). Petascale high order dynamic rupture earthquake simulations on heterogeneous supercomputers. In *Sc '14: Proceedings of the international conference for high performance computing, networking, storage and analysis* (p. 3-14). doi: 10.1109/SC.2014.6

Jia, Z., Jin, Z., Marchandon, M., Ulrich, T., Gabriel, A.-A., Fan, W., ... Fialko, Y. (2023). The complex dynamics of the 2023 Kahramanmaraş, Turkey, Mw 7.8-7.7 earthquake doublet. *Science*, *0*, eadi0685. doi: 10.1126/science.adi0685

Krenz, L., Uphoff, C., Ulrich, T., Gabriel, A.-A., Abrahams, L. S., Dunham, E. M., & Bader, M. (2021). 3D Acoustic-Elastic Coupling with Gravity: The Dynamics of the 2018 Palu, Sulawesi Earthquake and Tsunami. In *Proceedings of the International Conference for High Performance Computing, Networking, Storage and Analysis*. New York, NY, USA: Association for Computing Machinery. doi: 10.1145/3458817.3476173

Käser, M., & Dumbser, M. (2006, 08). An arbitrary high-order discontinuous Galerkin method for elastic waves on unstructured meshes — I. The two-dimensional isotropic

case with external source terms. *Geophysical Journal International*, 166(2), 855-877.  
doi: 10.1111/j.1365-246X.2006.03051.x

Leprince, S., Barbot, S., Ayoub, F., & Avouac, J.-P. (2007). Automatic and precise orthorectification, coregistration, and subpixel correlation of satellite images, application to ground deformation measurements. *IEEE Transactions on Geoscience and Remote Sensing*, 45(6), 1529–1558.

Ma, S. (2008). A physical model for widespread near-surface and fault zone damage induced by earthquakes. *Geochemistry, Geophysics, Geosystems*, 9(11). doi: 10.1029/2008GC002231

Madden, E. H., Ulrich, T., & Gabriel, A.-A. (2022). The State of Pore Fluid Pressure and 3-D Megathrust Earthquake Dynamics. *Journal of Geophysical Research: Solid Earth*, 127(4), e2021JB023382. Retrieved from <https://agupubs.onlinelibrary.wiley.com/doi/abs/10.1029/2021JB023382> (e2021JB023382 2021JB023382)  
doi: 10.1029/2021JB023382

Pelties, C., de la Puente, J., Ampuero, J.-P., Brietzke, G. B., & Käser, M. (2012). Three-dimensional dynamic rupture simulation with a high-order discontinuous galerkin method on unstructured tetrahedral meshes. *Journal of Geophysical Research: Solid Earth*, 117(B2). doi: 10.1029/2011JB008857

Pelties, C., Gabriel, A.-A., & Ampuero, J.-P. (2014). Verification of an ADER-DG method for complex dynamic rupture problems. *Geoscientific Model Development*, 7(3), 847–866. doi: 10.5194/gmd-7-847-2014

Scholz, C. H. (1988, Feb 01). The brittle-plastic transition and the depth of seismic faulting. *Geologische Rundschau*, 77(1), 319-328. doi: 10.1007/BF01848693

Simmetrix Inc. (2017). *Simmodeler: Simulation modeling suite 11.0 documentation* (Tech. Rep.). Simmetrix Inc.

- Taufiqurrahman, T., Gabriel, A.-A., Li, D., Ulrich, T., Li, B., Carena, S., ... Gallovič, F. (2023, Jun 01). Dynamics, interactions and delays of the 2019 Ridgecrest rupture sequence. *Nature*, *618*(7964), 308-315. doi: 10.1038/s41586-023-05985-x
- Templeton, E. L., & Rice, J. R. (2008). Off-fault plasticity and earthquake rupture dynamics: 1. Dry materials or neglect of fluid pressure changes. *Journal of Geophysical Research: Solid Earth*, *113*(B09306). doi: 10.1029/2007JB005529
- Thollard, F., Clesse, D., Doin, M.-P., Donadieu, J., Durand, P., Grandin, R., ... others (2021). Flatsim: The form@ter large-scale multi-temporal sentinel-1 interferometry service. *Remote Sensing*, *13*(18), 3734.
- Tinti, E., Casarotti, E., Ulrich, T., Taufiqurrahman, T., Li, D., & Gabriel, A.-A. (2021). Constraining families of dynamic models using geological, geodetic and strong ground motion data: The Mw 6.5, October 30th, 2016, Norcia earthquake, Italy. *Earth and Planetary Science Letters*, *576*, 117237. doi: 10.1016/j.epsl.2021.117237
- Ulrich, T., Gabriel, A.-A., Ampuero, J.-P., & Xu, W. (2019). Dynamic viability of the 2016 Mw 7.8 Kaikōura earthquake cascade on weak crustal faults. *Nature communications*, *10*(1), 1213. doi: 10.1038/s41467-019-09125-w
- Uphoff, C., Rettenberger, S., Bader, M., Madden, E. H., Ulrich, T., Wollherr, S., & Gabriel, A.-A. (2017). Extreme scale multi-physics simulations of the tsunamigenic 2004 sumatra megathrust earthquake. In *Proceedings of the international conference for high performance computing, networking, storage and analysis*. New York, NY, USA: Association for Computing Machinery. doi: 10.1145/3126908.3126948
- USGS. (2021). *Overview: M7.3 - Southern Qinghai, China*. Retrieved from <https://earthquake.usgs.gov/earthquakes/eventpage/us7000e54r/executive>
- Wang, M., Wang, F., Jiang, X., Tian, J., Li, Y., Sun, J., & Shen, Z.-K. (2021, 11). GPS determined coseismic slip of the 2021 Mw 7.4 Maduo, China, earthquake and

- its tectonic implication. *Geophysical Journal International*, 228(3), 2048-2055. doi: 10.1093/gji/ggab460
- Wollherr, S., Gabriel, A.-A., & Mai, P. M. (2019). Landers 1992 “reloaded”: Integrative dynamic earthquake rupture modeling. *Journal of Geophysical Research: Solid Earth*, 124(7), 6666-6702. doi: 10.1029/2018JB016355
- Wollherr, S., Gabriel, A.-A., & Uphoff, C. (2018). Off-fault plasticity in three-dimensional dynamic rupture simulations using a modal Discontinuous Galerkin method on unstructured meshes: Implementation, verification and application. *Geophysical Journal International*, 214(3), 1556–1584. doi: 10.1093/GJI/GGY213
- Xin, H., Zhang, H., Kang, M., He, R., Gao, L., & Gao, J. (2018, 10). High-Resolution Lithospheric Velocity Structure of Continental China by Double-Difference Seismic Travel-Time Tomography. *Seismological Research Letters*, 90(1), 229-241. doi: 10.1785/0220180209
- Zinke, R., Hollingsworth, J., Dolan, J. F., & Van Dissen, R. (2019). Three-dimensional surface deformation in the 2016 MW 7.8 Kaikōura, New Zealand, earthquake from optical image correlation: Implications for strain localization and long-term evolution of the Pacific-Australian plate boundary. *Geochemistry, Geophysics, Geosystems*, 20(3), 1609–1628. doi: 10.1029/2018GC007951

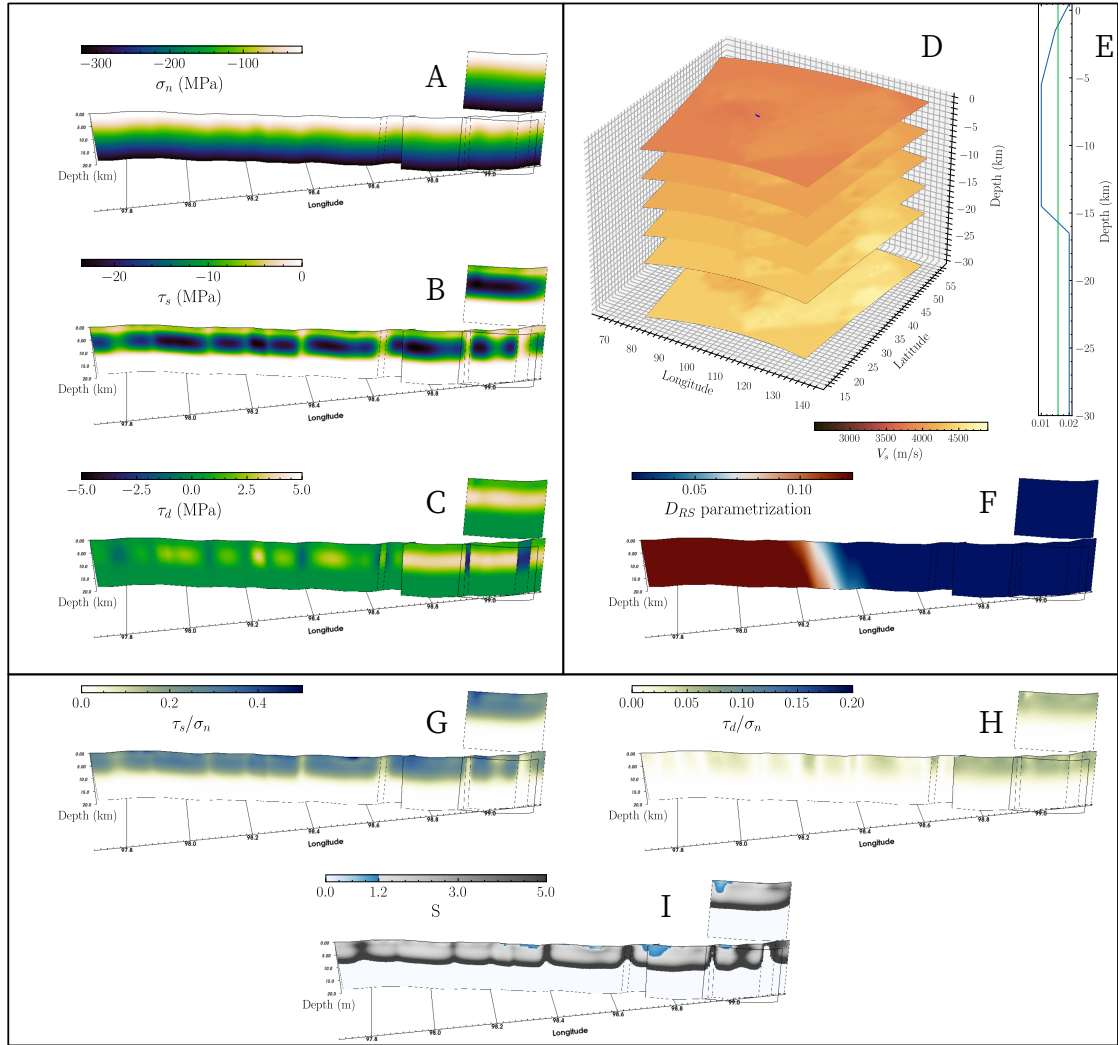


**Figure S1.** Initial conditions of the preferred 3D dynamic rupture model. Here, we show the initial stress components acting on-fault, combining the geodetically inferred stress heterogeneity and the ambient regional stresses (Table S1). (A) initial shear stress along-strike, (B) initial shear stress along-dip, (C) initial normal stress. (D) Cross-sections of the 3D velocity structure above a depth of 30 km (Xin et al., 2018) with the fault system marked in blue. (E) Depth-dependent fast-velocity weakening rate-and-state frictional parameters  $a$  (blue) and  $b$  (green). (F) along-strike variable  $D_{RS}$ , linearly increasing with horizontal distance from the epicenter to the North. The range of  $D_{RS}$  is given in **Table S1**. (G) ratio of initial along-strike shear stress to normal stress. (H) ratio of initial along-dip shear stress to normal stress. (I) the  $S$  ratio parameter that characterizes the relative fault strength governing dynamic rupture propagation and arrest by balancing fracture energy and strain energy release.

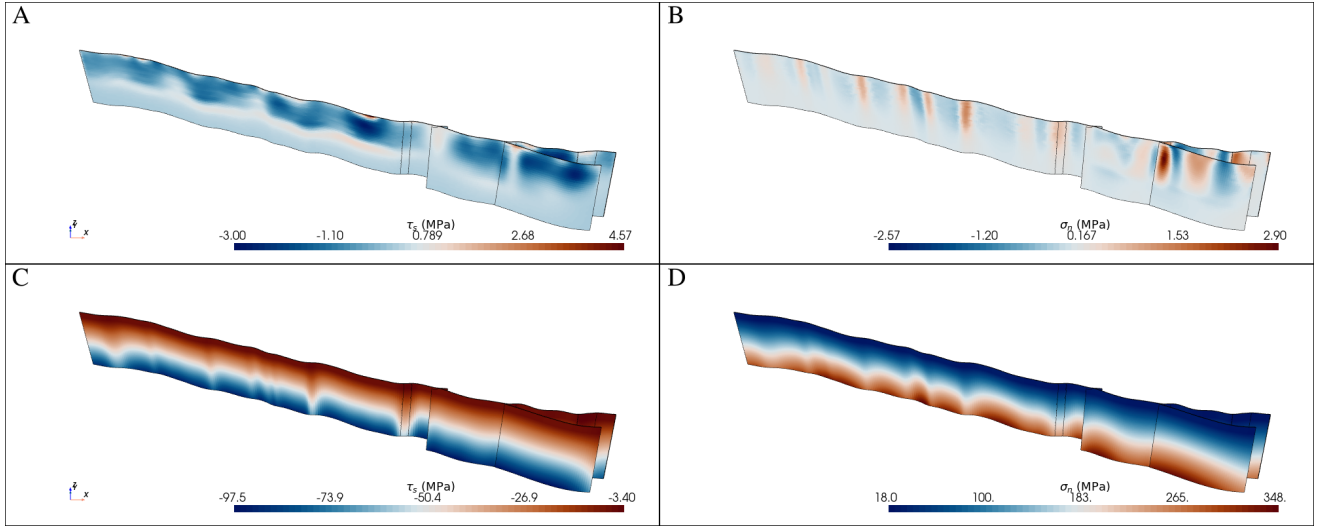


**Figure S2.** Geodetically-derived heterogeneous stresses and ambient tectonic stresses. (A) and (B) show the strike component of the shear stress change and the normal stress change, respectively, inferred from our geodetic slip model. The stress change distribution is already scaled by a factor of 0.3. (C) and (D) show the strike component of the ambient regional shear stress and the normal stress, respectively.

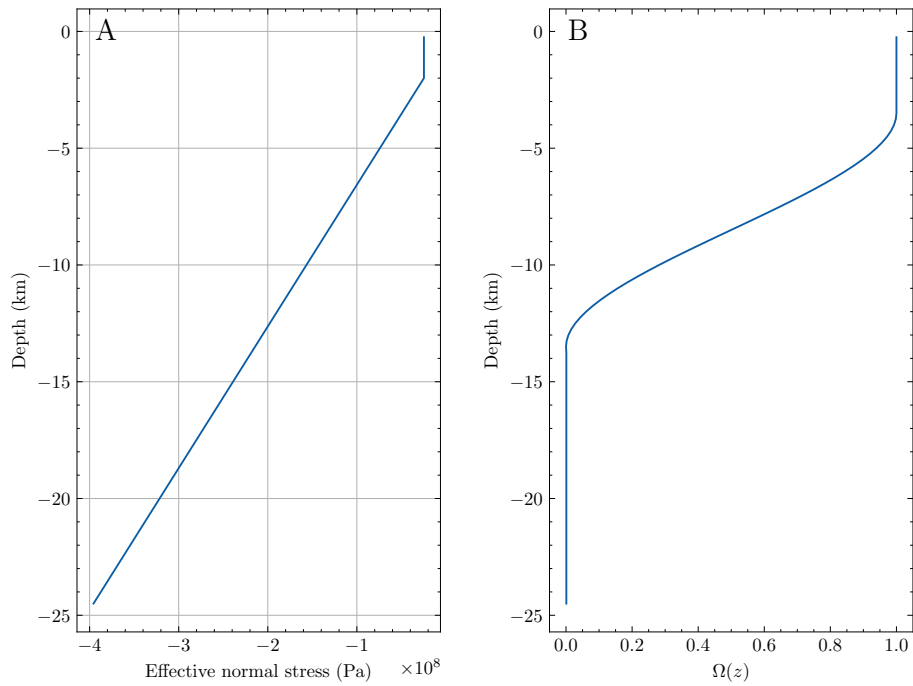


**Figure S3.** (A) Depth-dependence of the effective confining stress  $\sigma_c = (1 - \gamma)\sigma_z$ . (B) Depth-dependent stress modulation function  $\Omega_z$ .



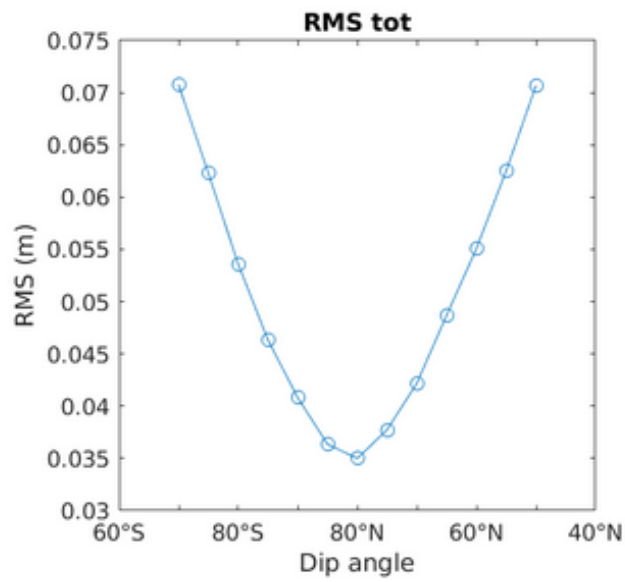


**Figure S4.** RMS misfit as a function of the dip angle assumed in the joint inversion (all segments have the same dip angle).

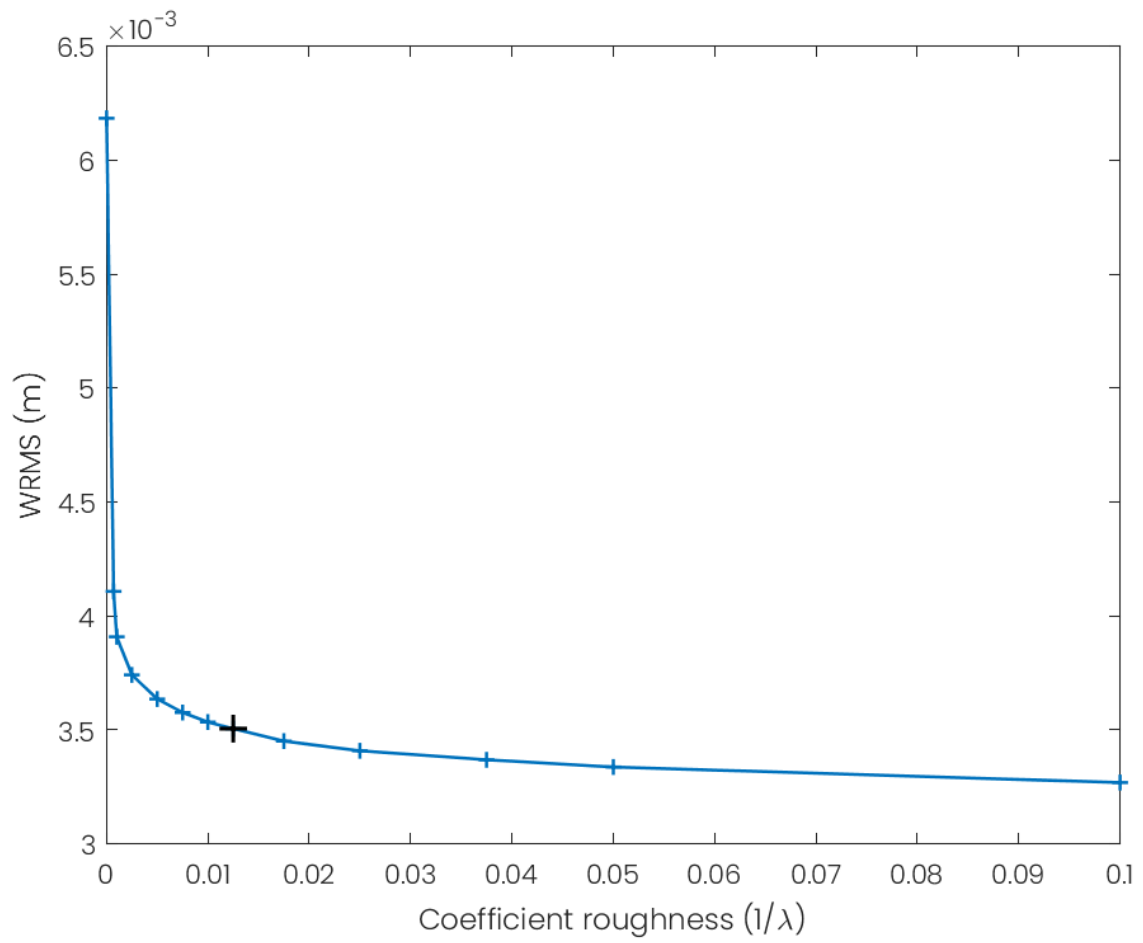


**Figure S5.** Data misfit as a function of roughness coefficient. The chosen roughness coefficient is indicated by the black cross.

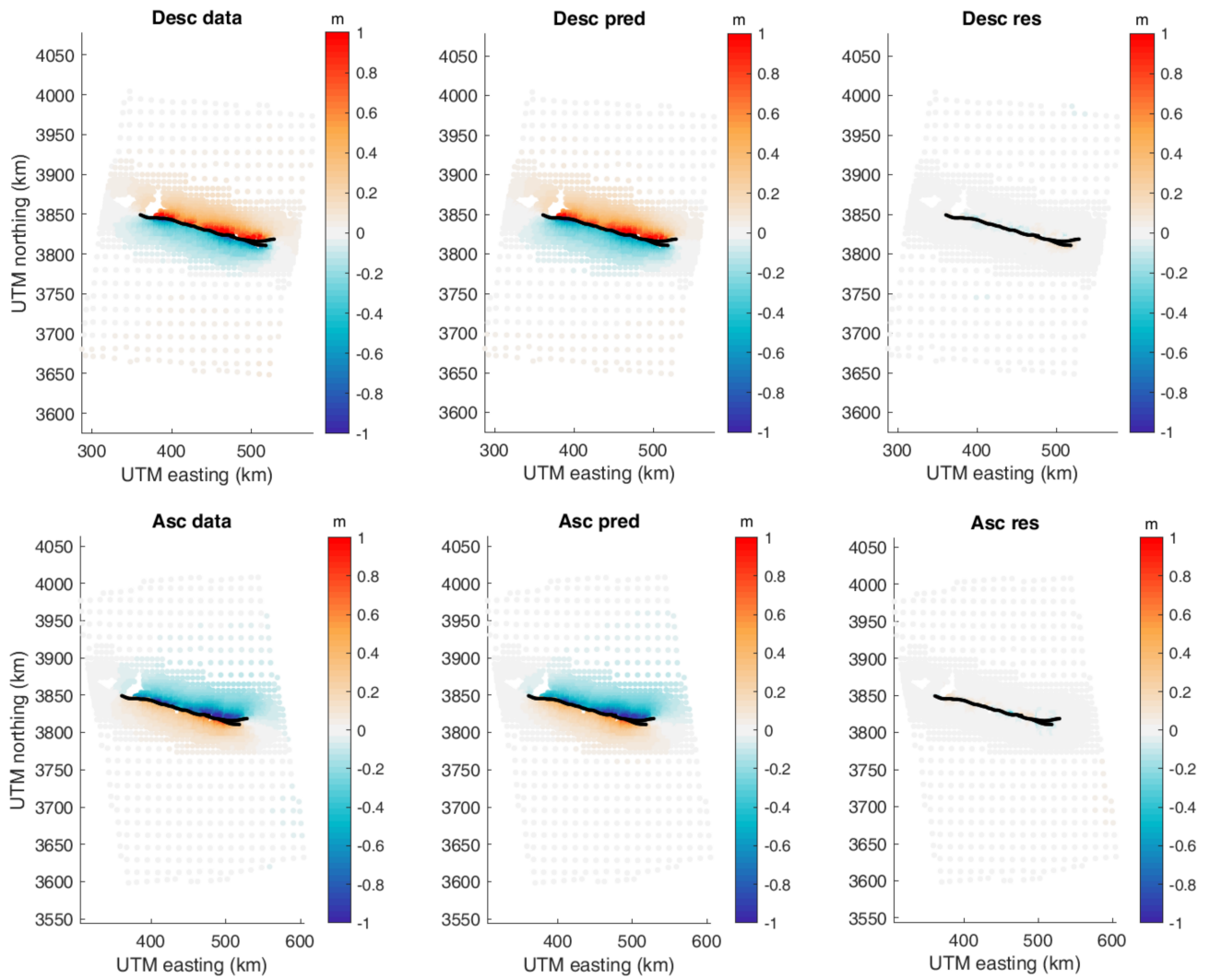


**Figure S6.** Data, predictions, and residuals for the descending (top) and ascending (bottom) interferograms.

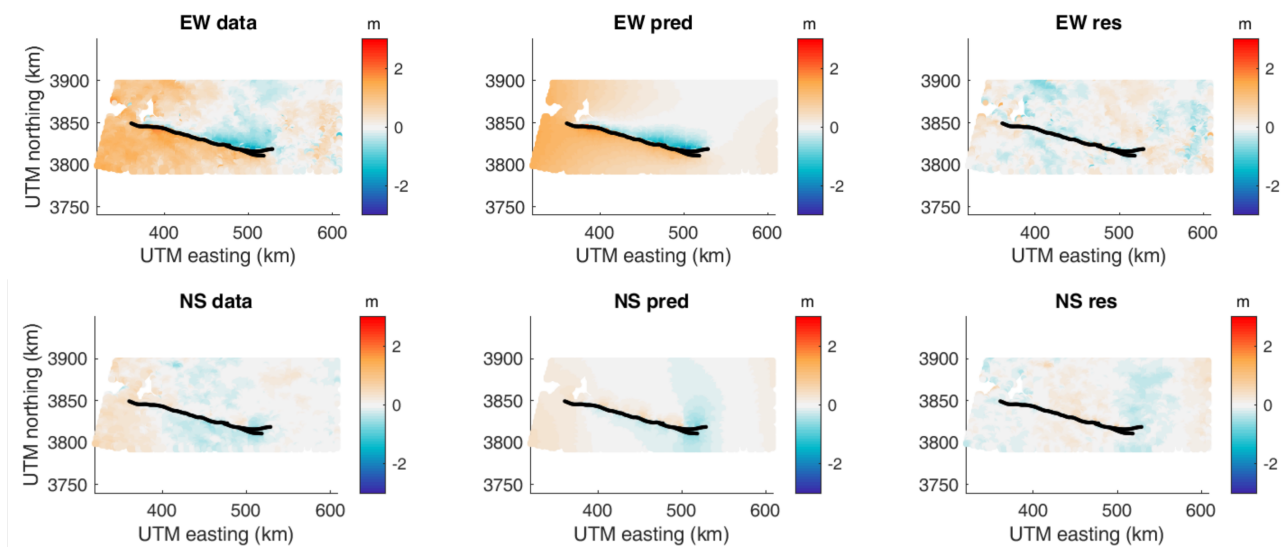


**Figure S7.** Data, predictions, and residuals for the EW (top) and NS (bottom) optical displacement fields.

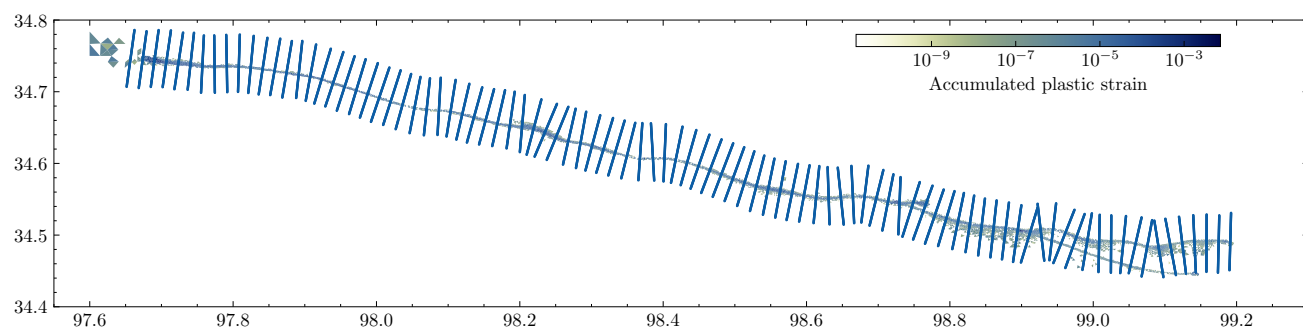


**Figure S8.** Fault-perpendicular surface transects sampling the off-fault plasticity field to the nearest cell-center values on the modeled surface of the preferred model.

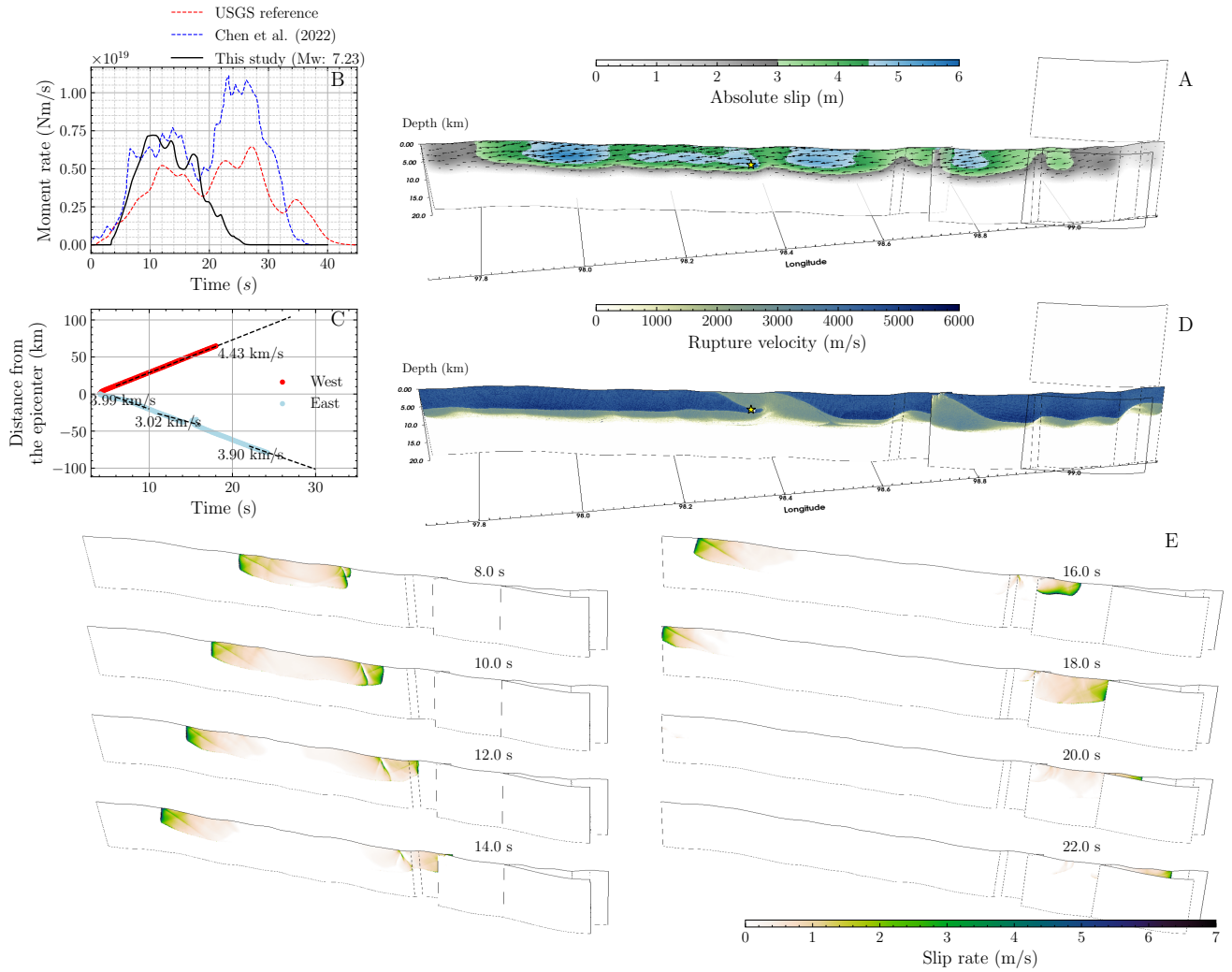


**Figure S9.** Same as main text Fig. 2 but for the alternative dynamic rupture model A1 with homogeneous  $D_{RS}=0.025$ .

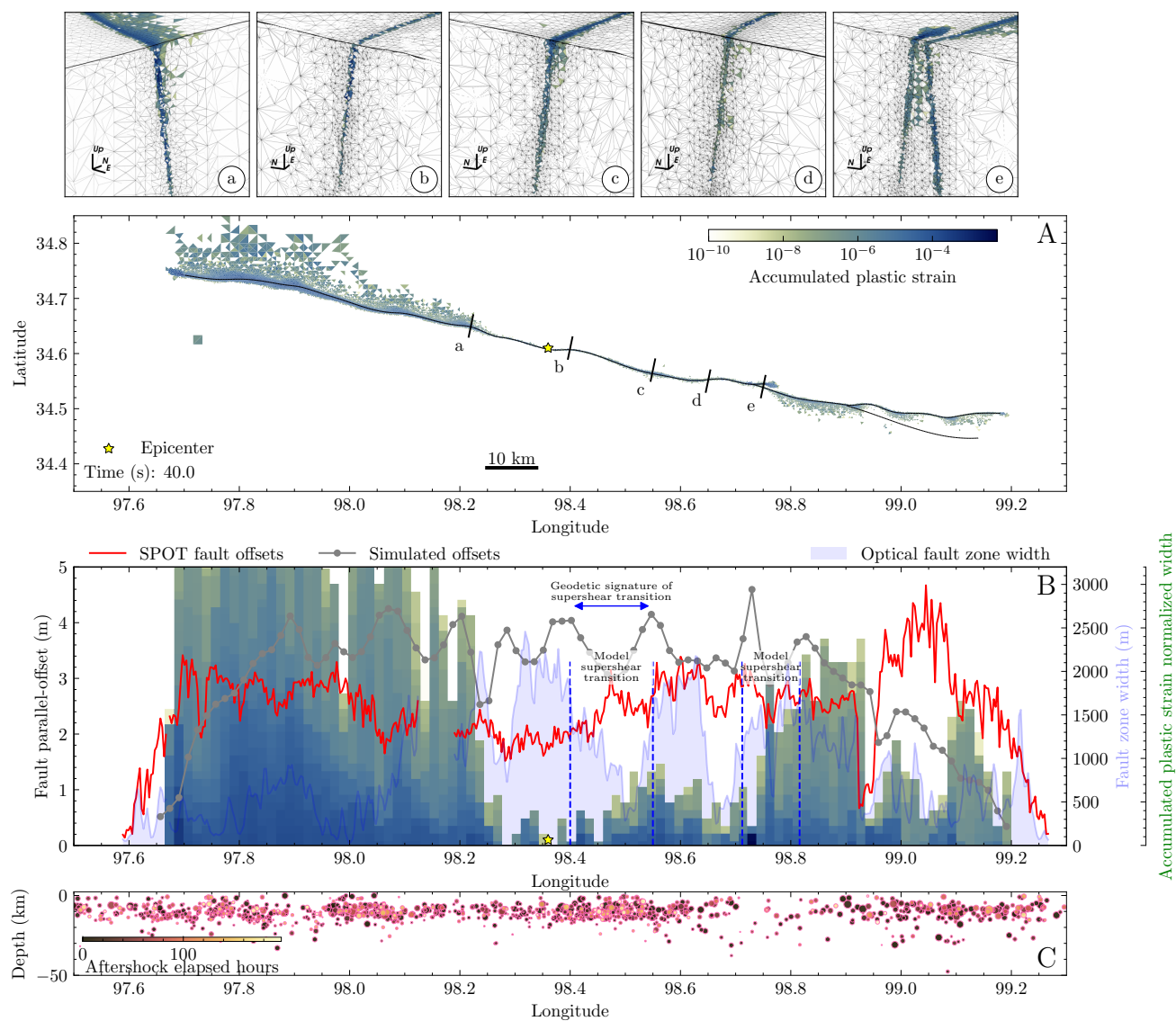


**Figure S10.** Same as main text Fig. 3 but for the alternative dynamic rupture model A1 with homogeneous  $D_{RS}=0.025$ .

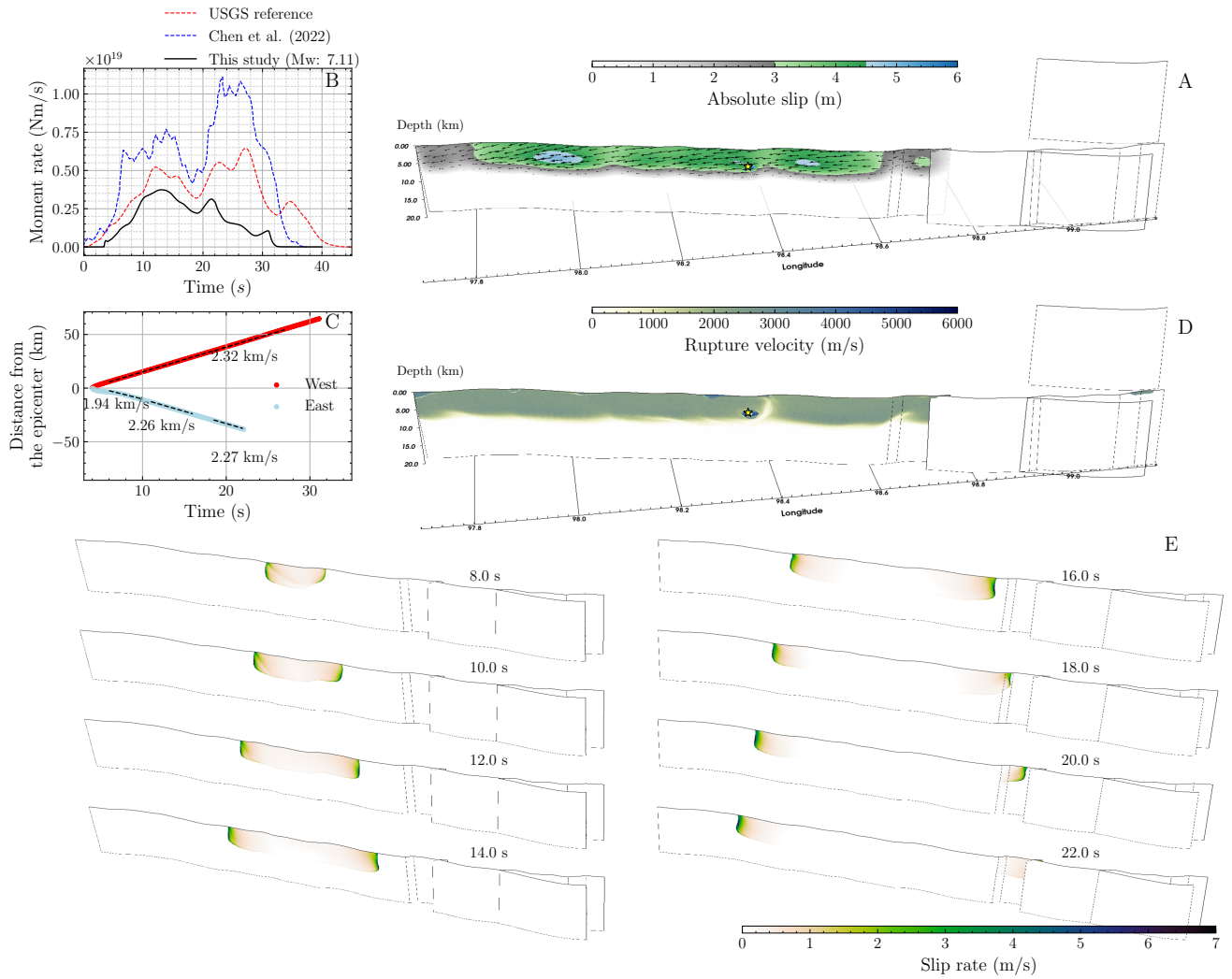


**Figure S11.** Same as main text Fig. 2 but for the alternative dynamic rupture A2 with homogeneous  $D_{RS}=0.125$ .

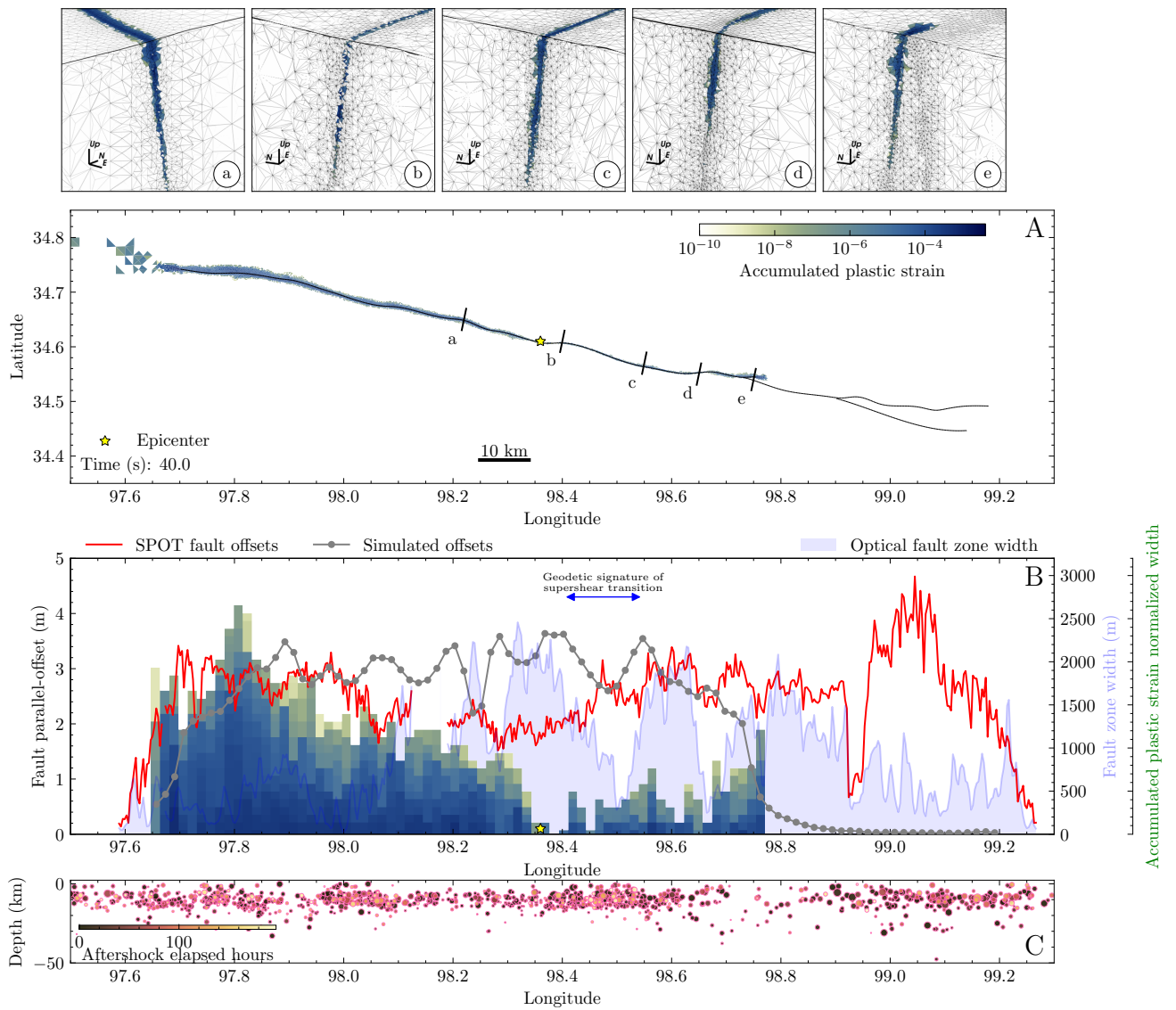


**Figure S12.** Same as main text Fig. 3 but for the alternative dynamic rupture but for model A2 with homogeneous  $D_{RS}=0.125$ .



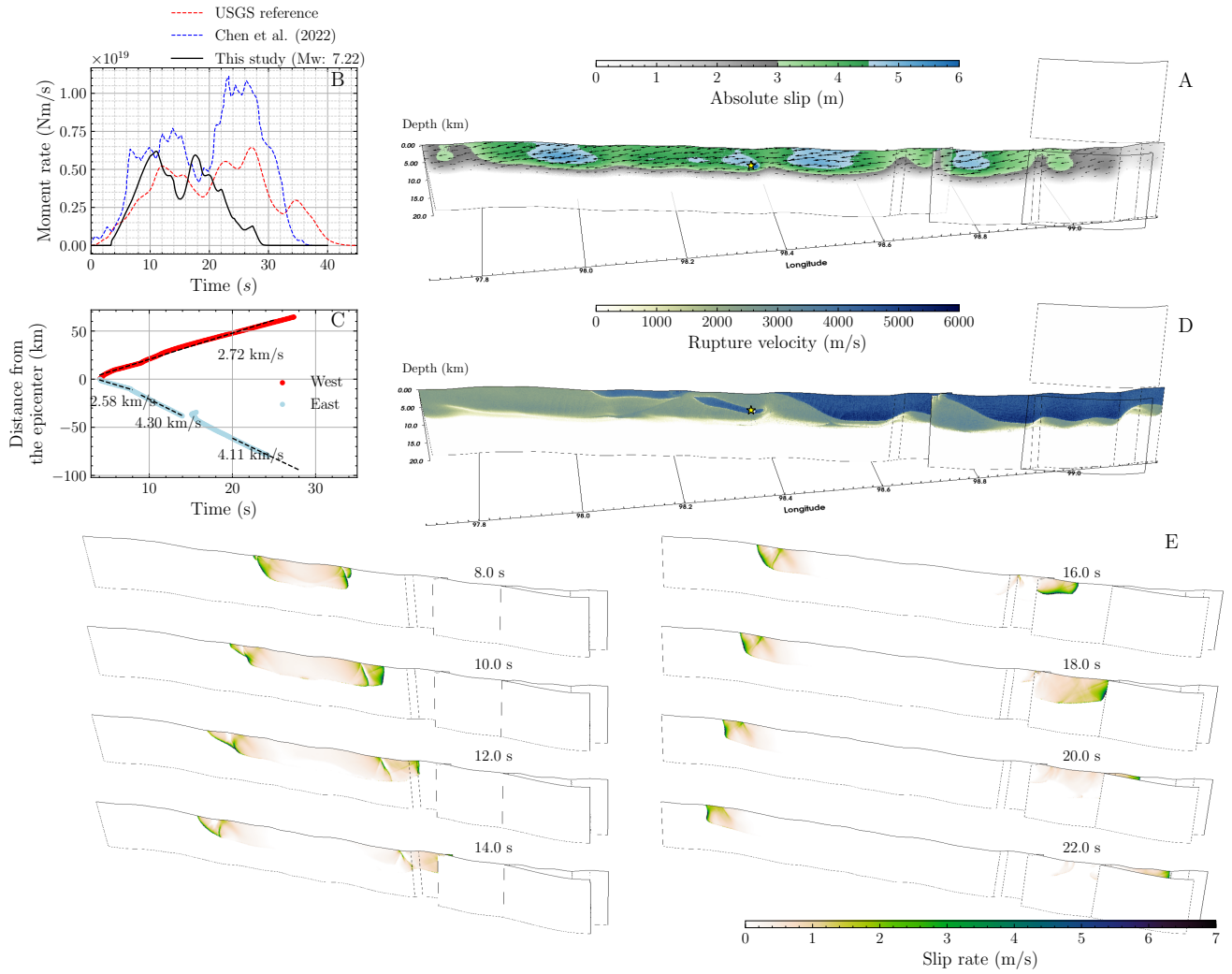


**Figure S13.** Same as main text Fig. 2 but for the alternative dynamic rupture model A3 with off-fault plastic cohesion  $C_{off} = 1 \times 10^{-4}\mu$ .

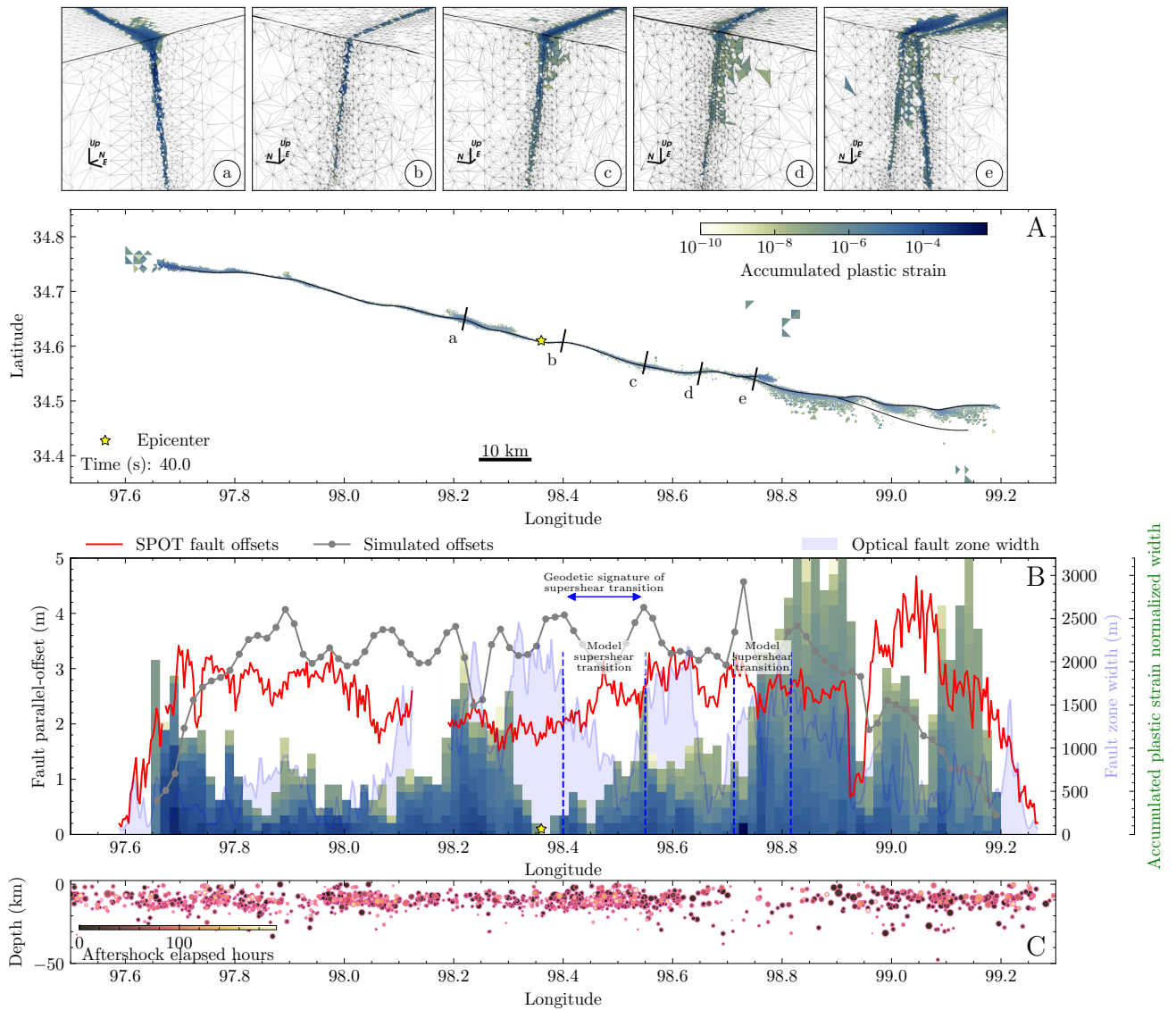


**Figure S14.** Same as main text Fig. 3 but for the alternative dynamic rupture model A3 with off-fault plastic cohesion  $C_{off} = 1 \times 10^{-4}\mu$ .

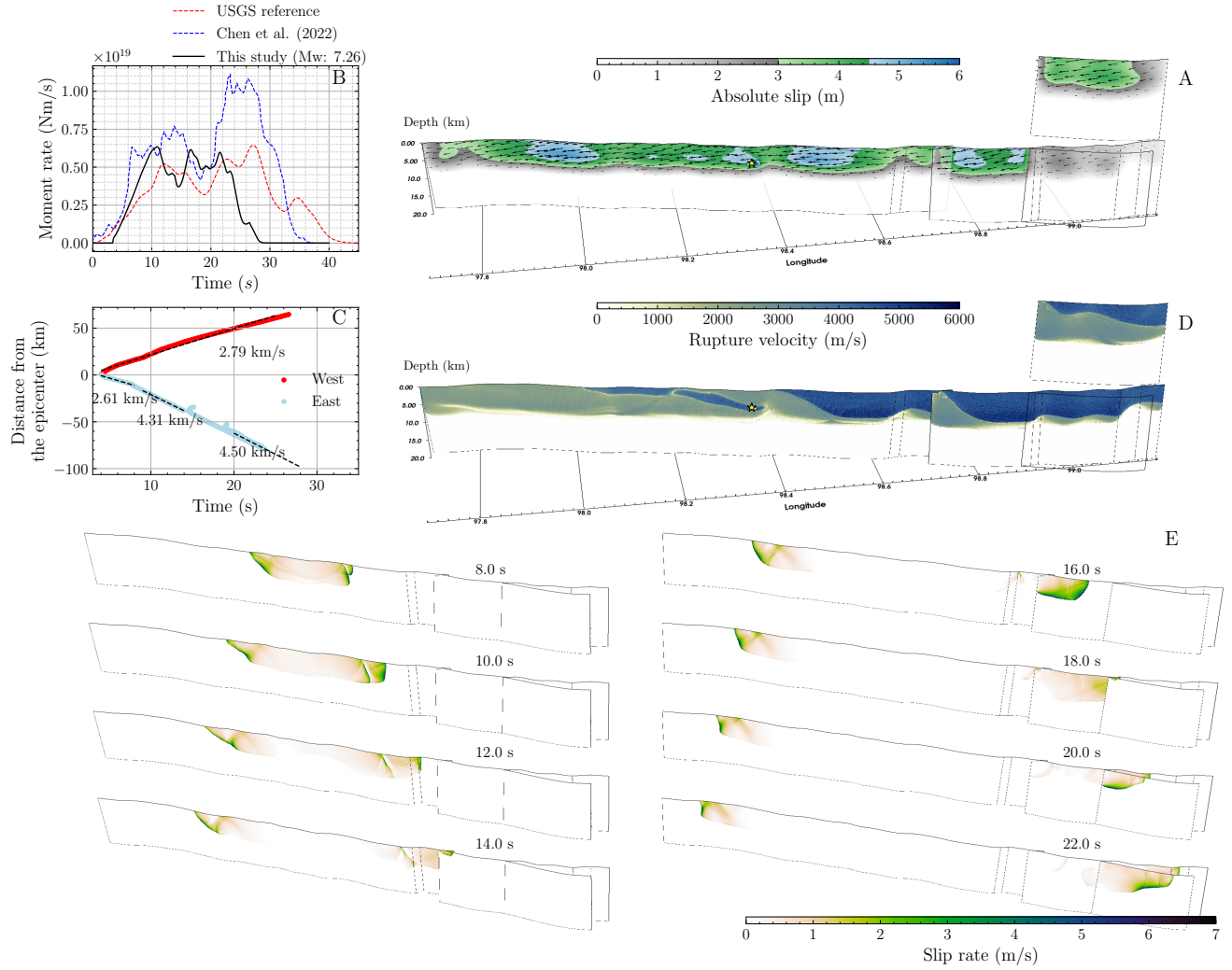


**Figure S15.** Same as main text Fig. 2 but for the alternative dynamic rupture model A4 with bulk plastic cohesion  $C_{off} = 5 \times 10^{-4}\mu$ .

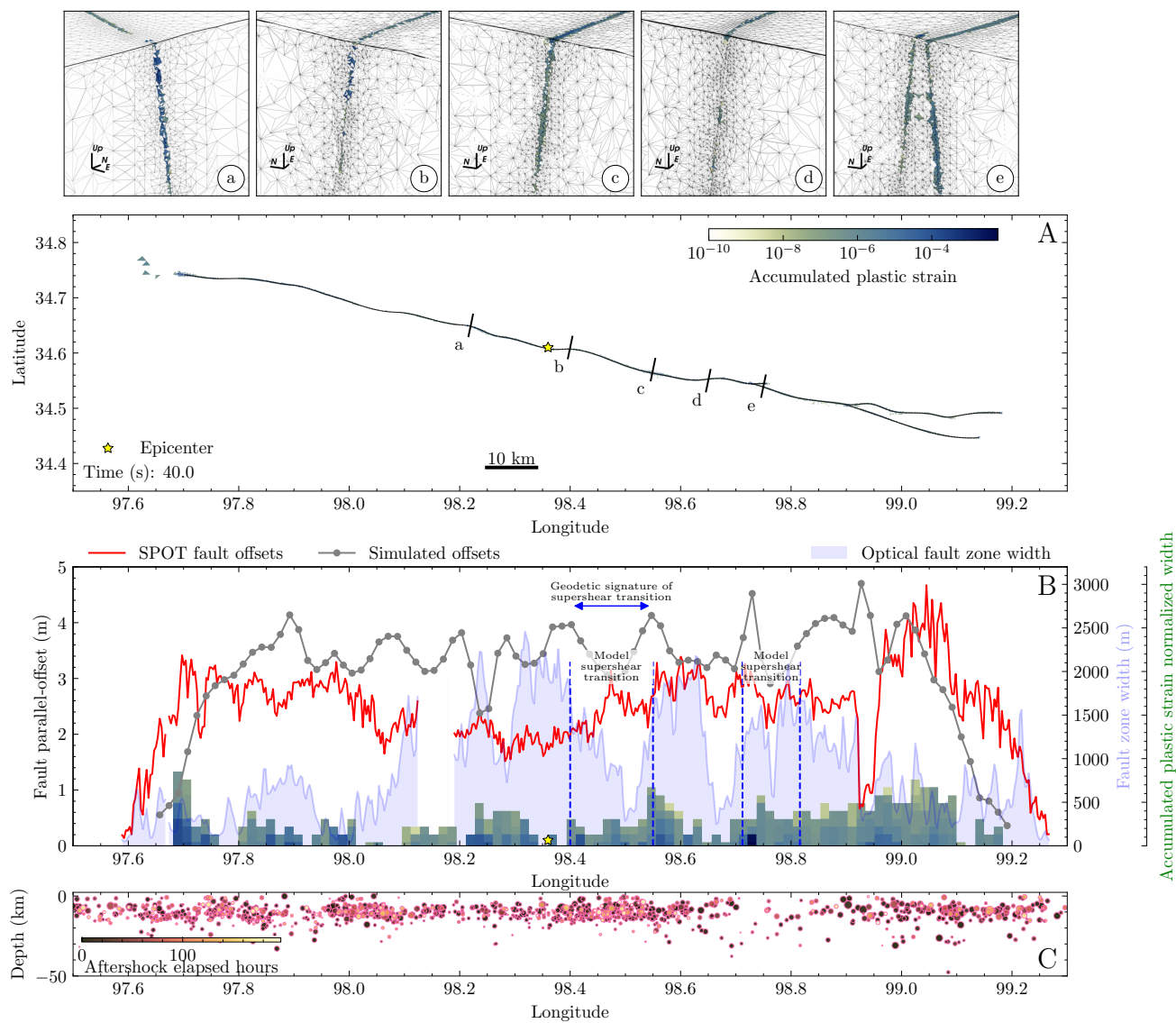


**Figure S16.** Same as main text Fig. 3 but for the alternative dynamic rupture model A4 with bulk plastic cohesion  $C_{off} = 5 \times 10^{-4} \mu$ .

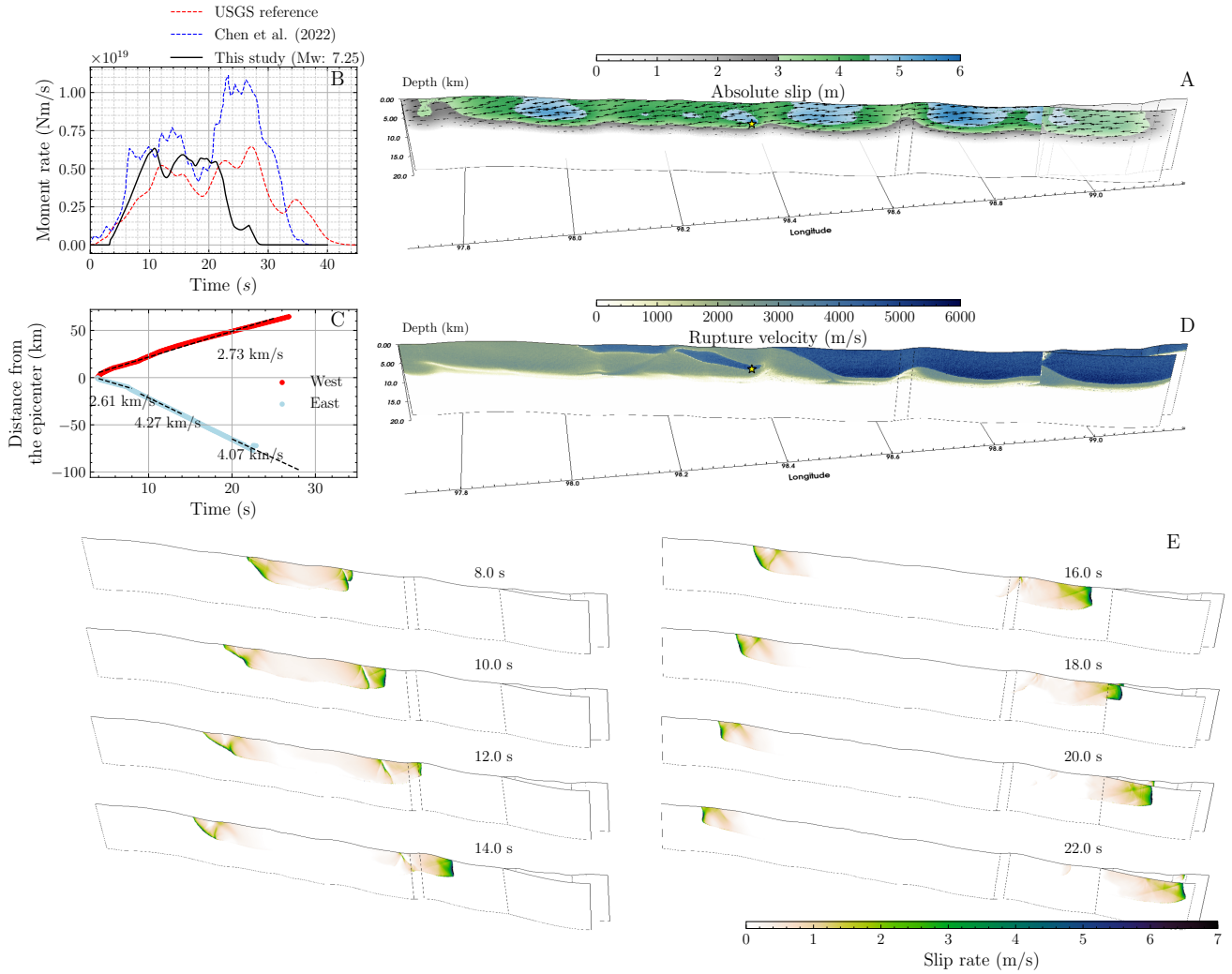


**Figure S17.** Same as main text Fig. 2 but for the alternative dynamic rupture model B1 in which the fault segments are all dipping northwards with  $83^\circ$ . The segments F1 and F2 of the preferred model are meshed continuously here, and thus, this model is composed of only two fault segments. The model uses the same parameter specifications as the preferred model.

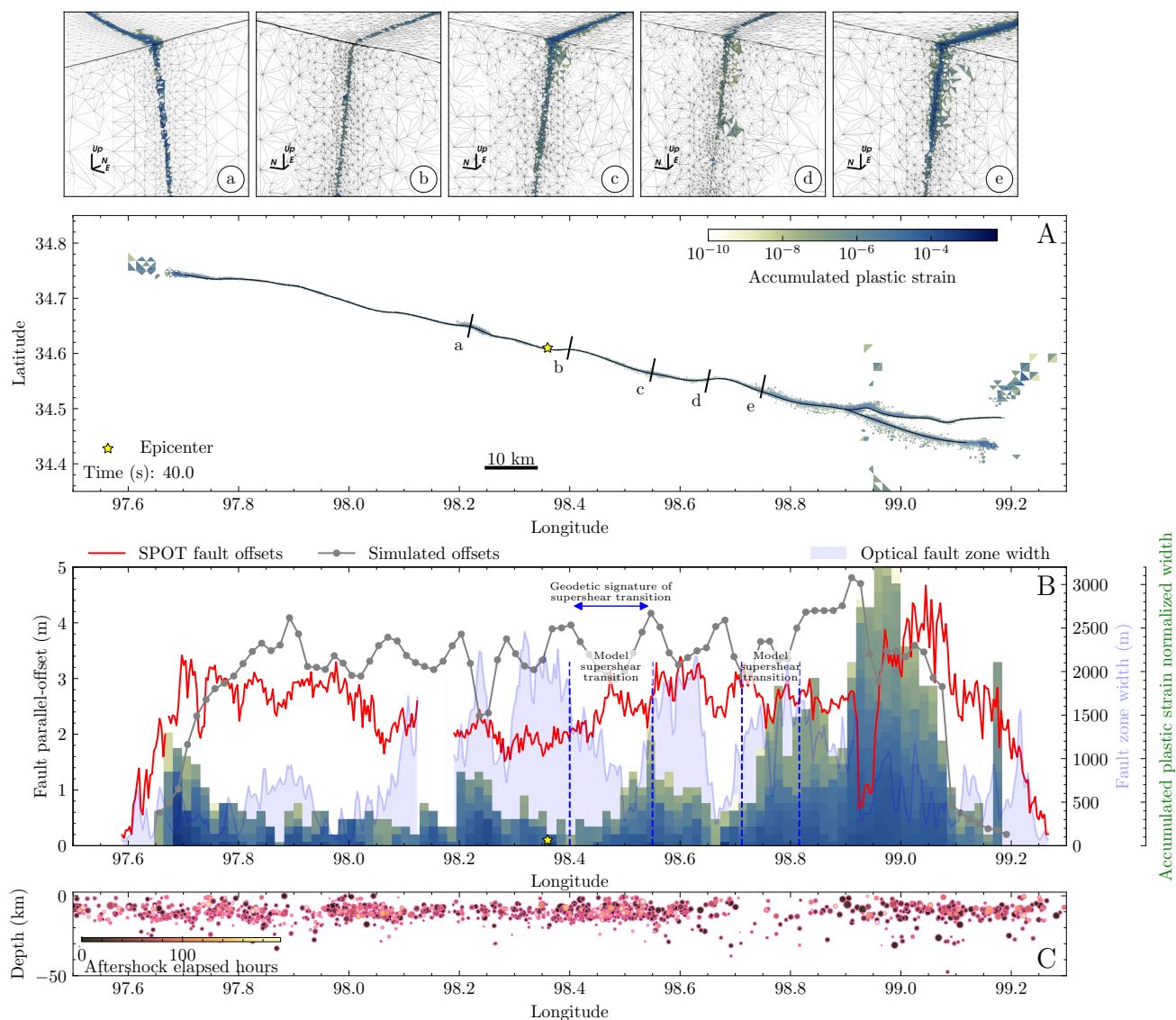


**Figure S18.** Same as main text Fig. 3 but for the alternative dynamic rupture model B1 in which the fault segments are all dipping northwards with  $83^\circ$ . The segments F1 and F2 of the preferred model are meshed continuously here, and thus, this model is composed of only two fault segments. The model uses the same parameter specifications as the preferred model.

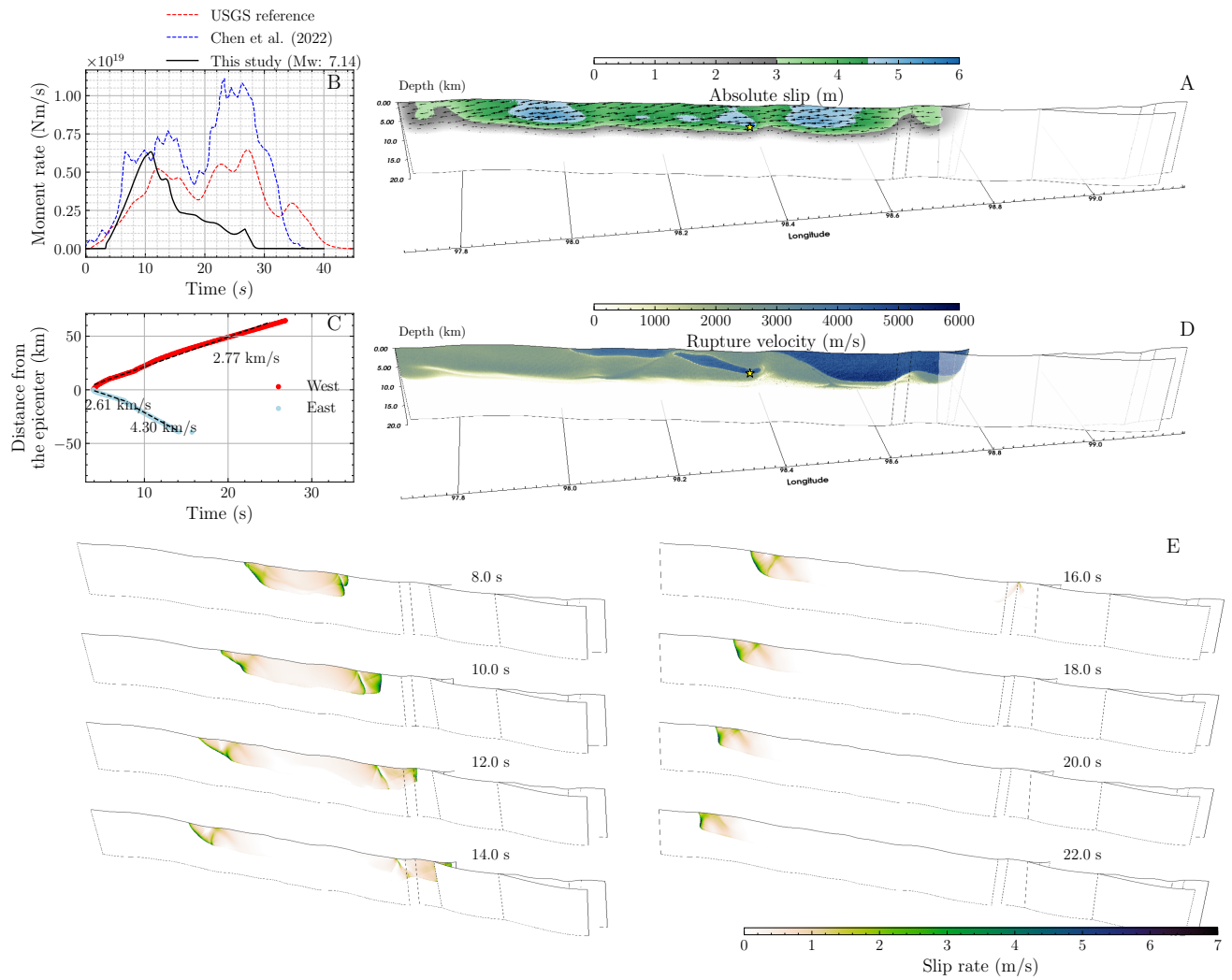


**Figure S19.** Same as main text Fig. 2 but for the alternative dynamic rupture model B2 in which the fault segments are all dipping northwards with  $83^\circ$ . The fault system is composed of three fault segments. All other parameters are the same as in the preferred model.

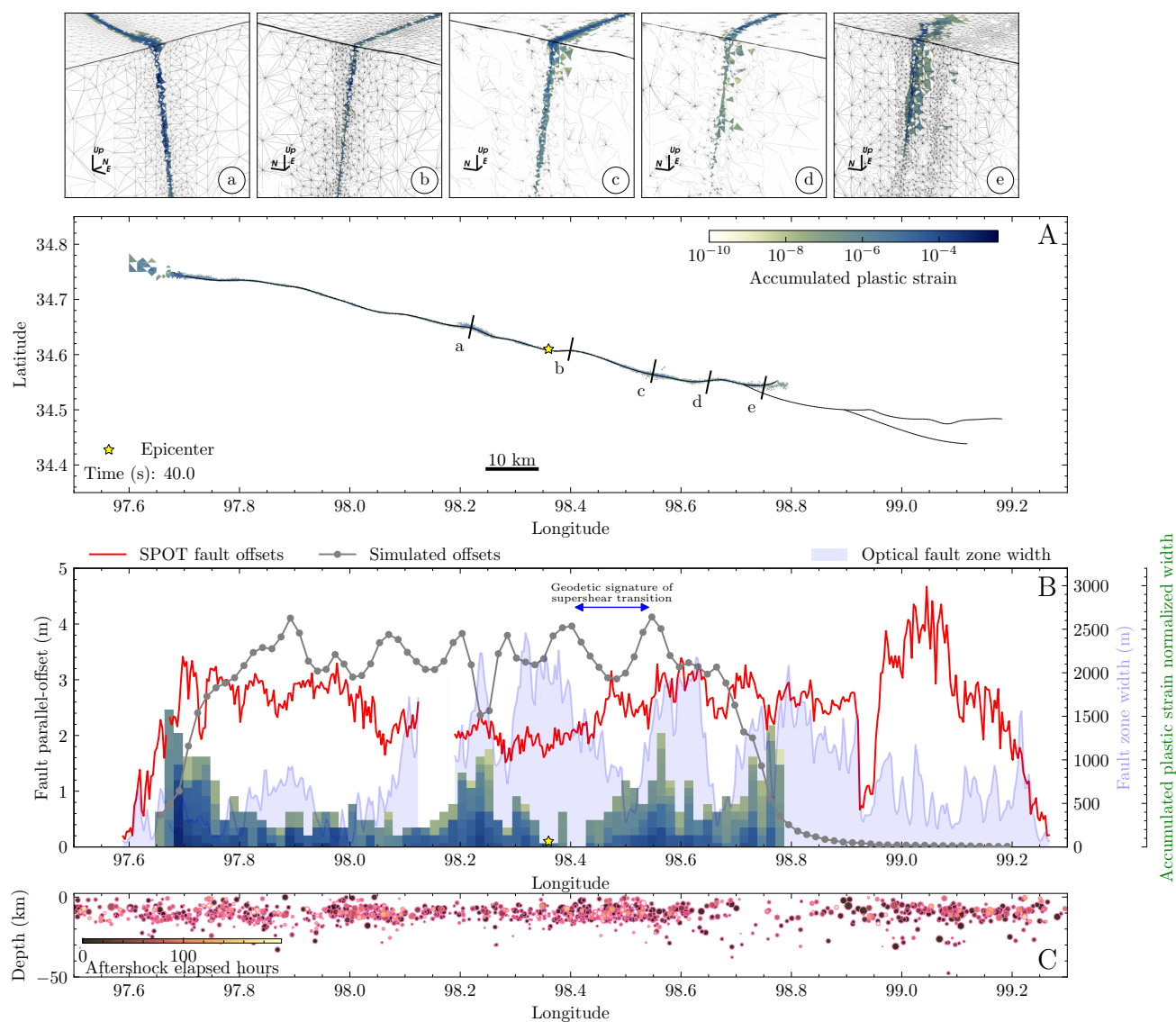


**Figure S20.** Same as main text Fig. 3 but for the alternative dynamic rupture model B2 in which the fault segments are all dipping northwards with  $83^\circ$ . The fault system is composed of three fault segments. All other parameters are the same as in the preferred model.



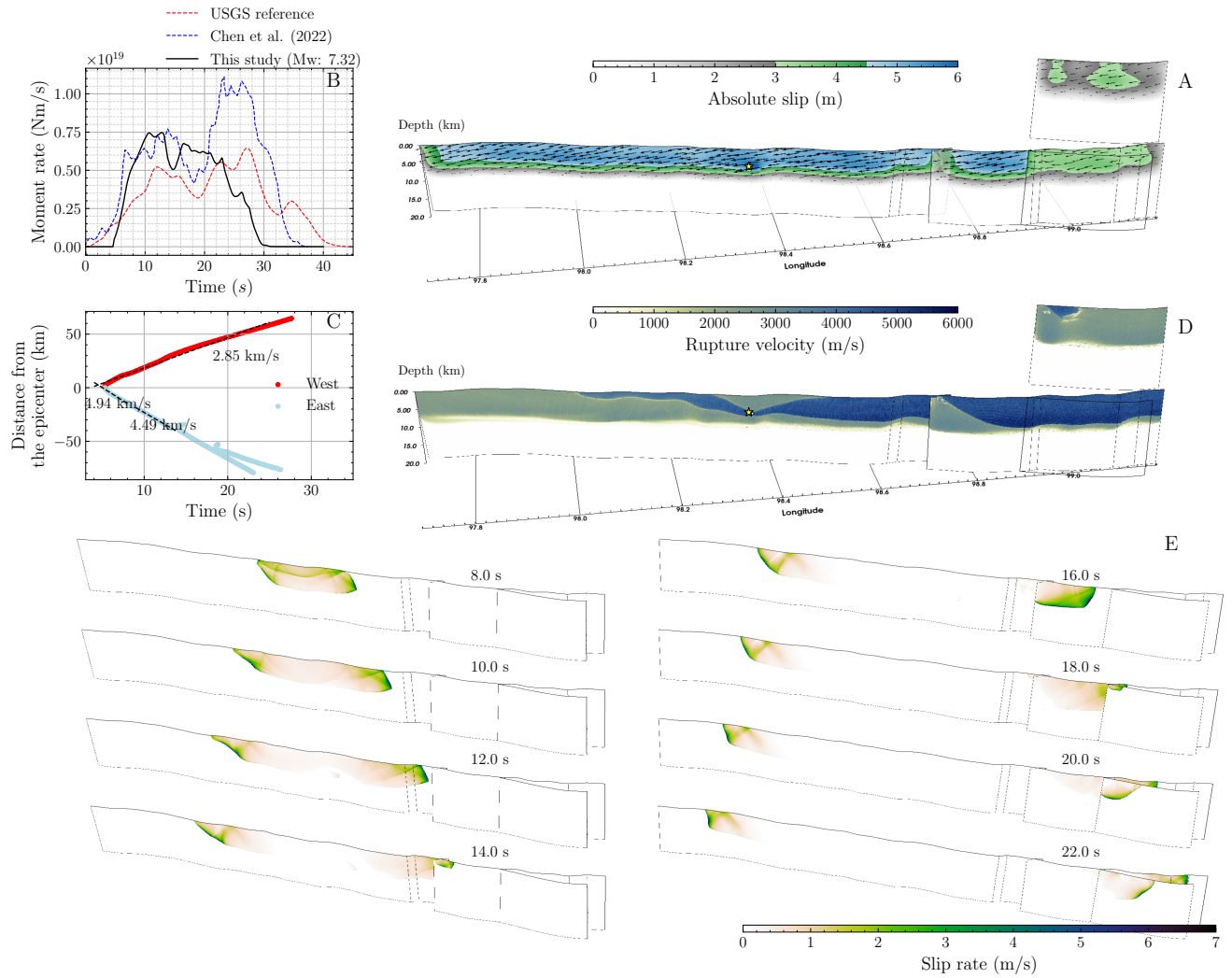


**Figure S21.** Same as main text Fig. 2 but for the alternative dynamic rupture model C1 with different ambient pre-stress, resulting in a  $100^\circ$  strike angle of an optimally oriented fault.

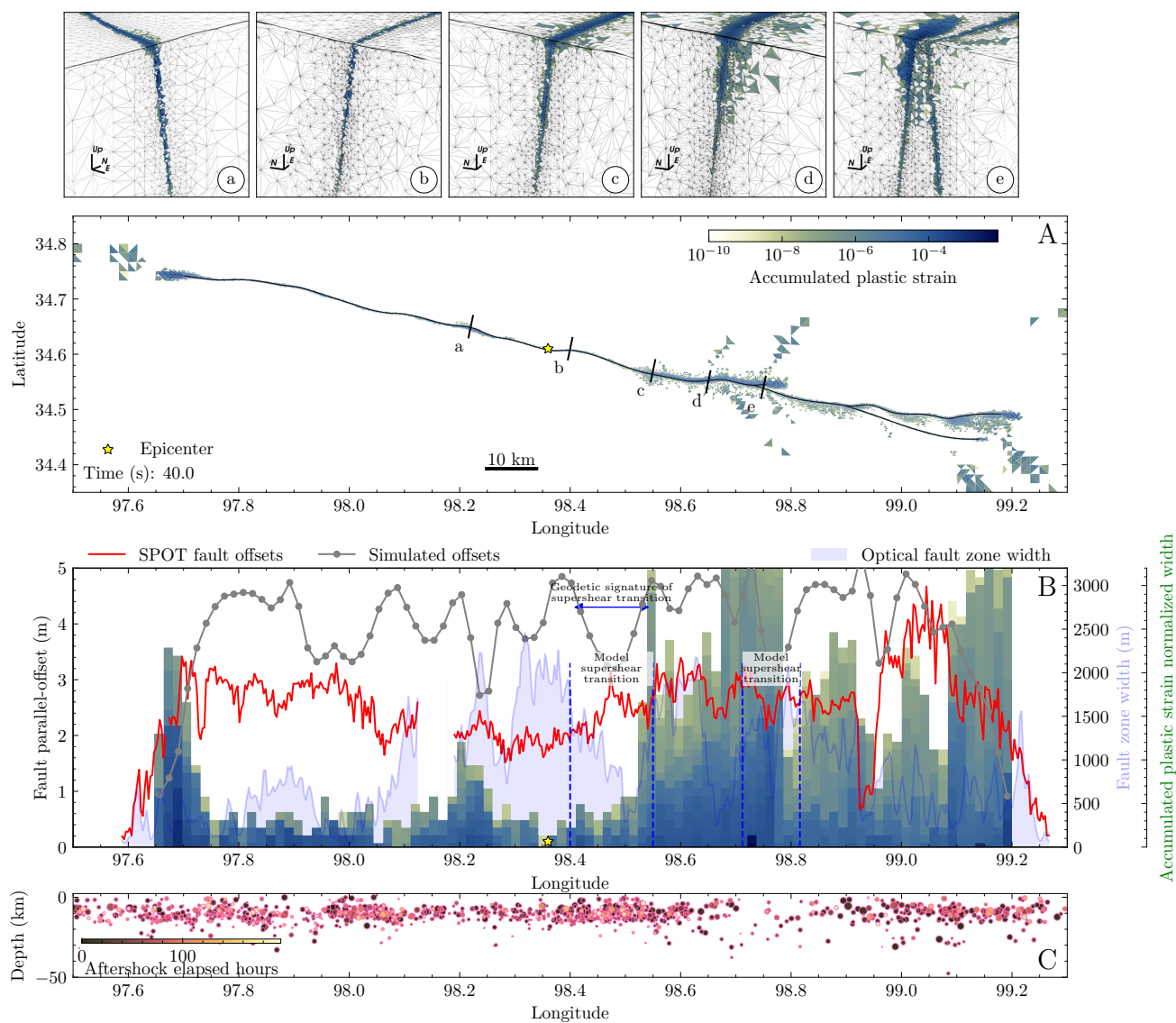


**Figure S22.** Same as main text Fig. 3 but for the alternative dynamic rupture model C1, with different ambient pre-stress, resulting in a  $100^\circ$  strike angle of an optimally oriented fault.

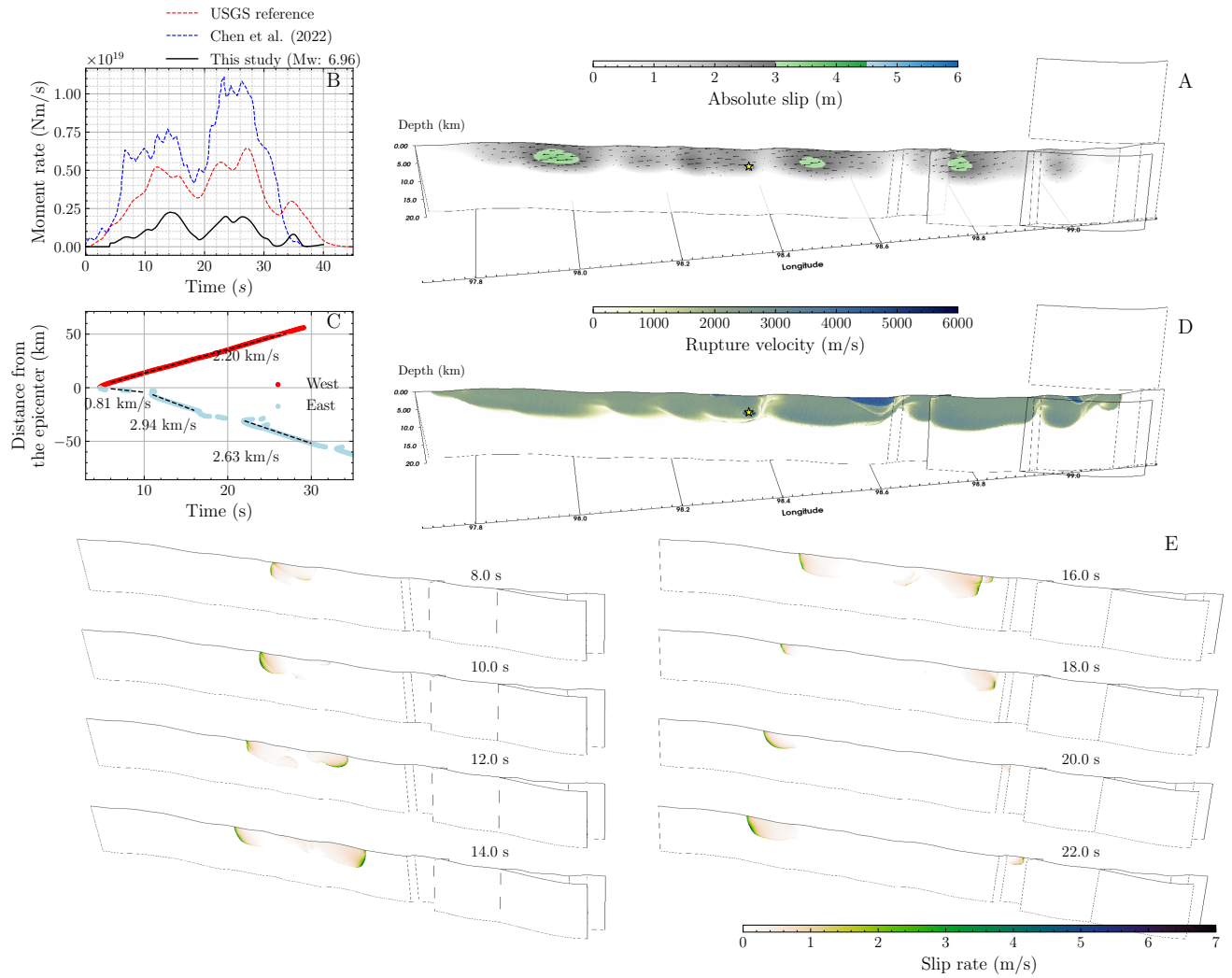


**Figure S23.** Same as main text Fig. 2 but for the alternative dynamic rupture model C2, with different ambient pre-stress, resulting in a  $120^\circ$  strike angle of an optimally oriented fault.

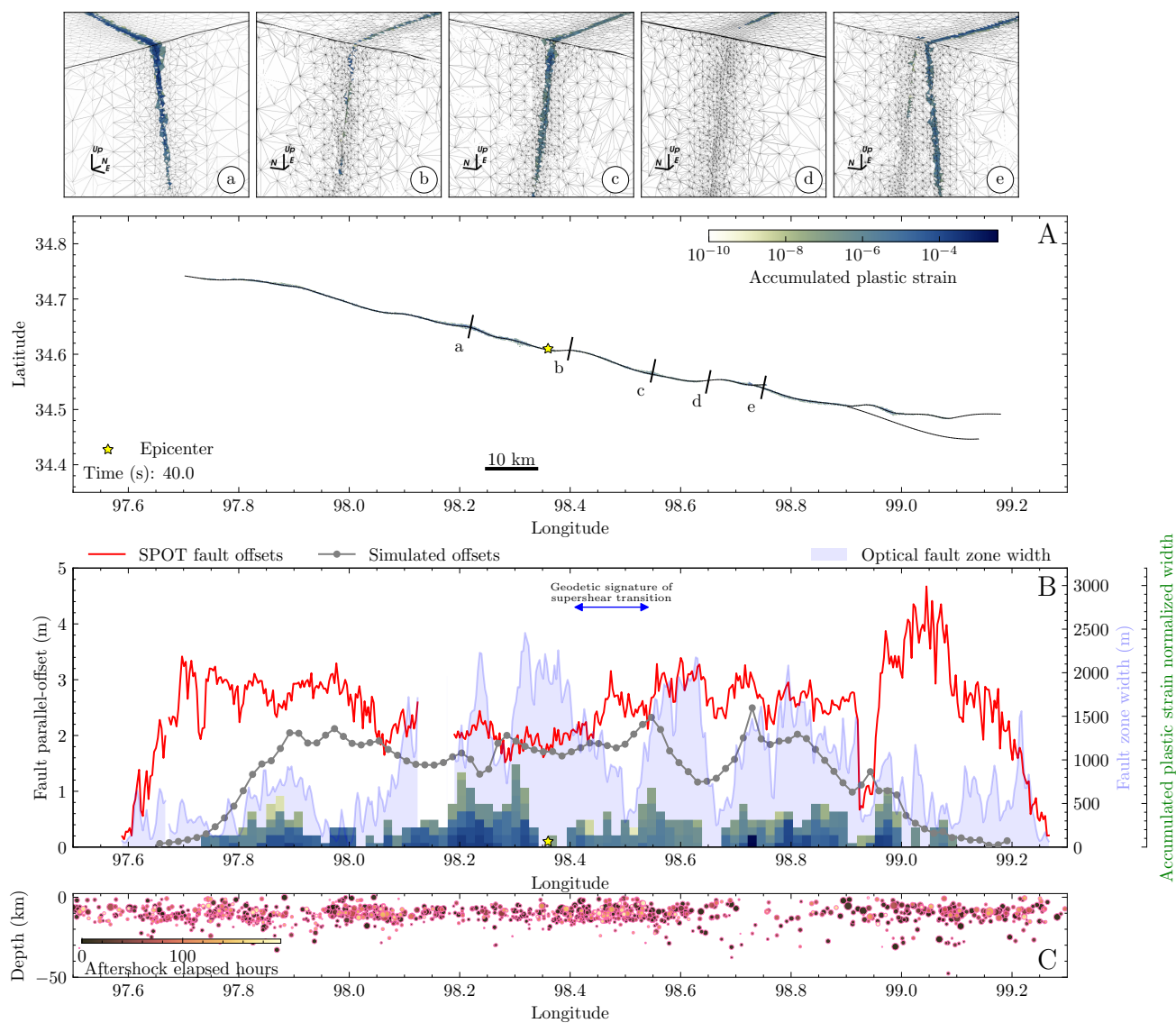


**Figure S24.** Same as main text Fig. 3 but for the alternative dynamic rupture model C2, with different ambient pre-stress, resulting in a  $120^\circ$  strike angle of an optimally oriented fault.

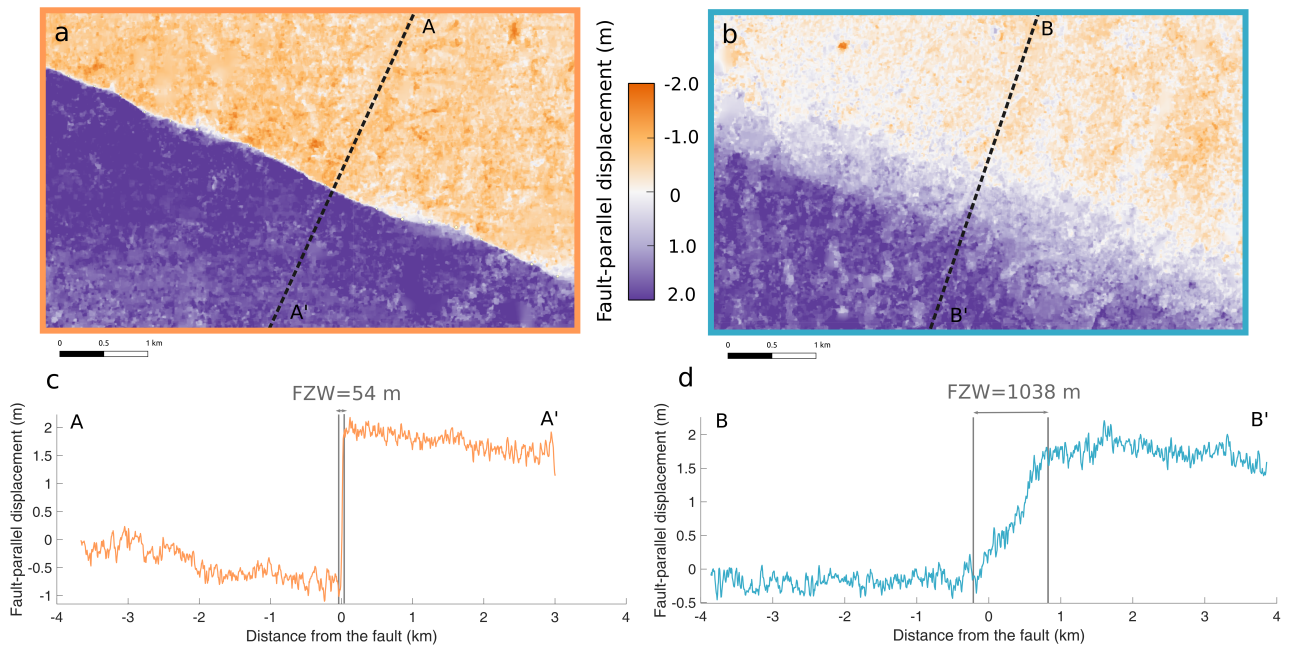


**Figure S25.** Close-up views of the fault-parallel surface displacement field and fault perpendicular profiles where the deformation is dominantly (A,C) localized versus (B,D) distributed. Black dotted lines in Figures A and B indicate the location of the profiles shown in panels C and D, respectively. The width of the region in the vicinity of the fault accommodating the deformation (the Fault Zone Width, FZW) is indicated by two vertical gray lines in Figures C and D, and the inferred value of the FZW is indicated on top. The location of the close-up views is indicated in Figure 1 of the main text.

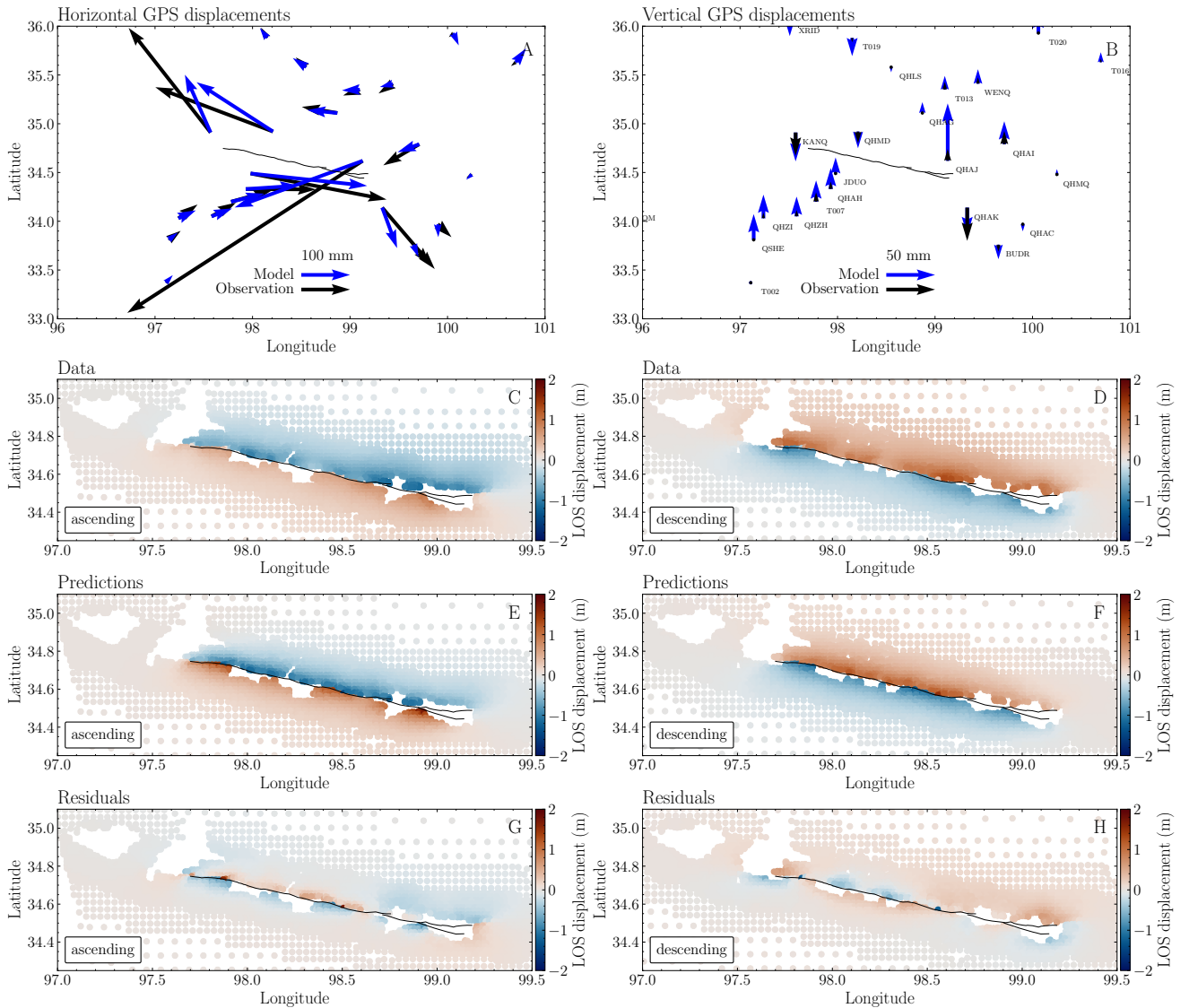


**Figure S26.** (A) Horizontal and (B) vertical components of the GPS displacements inferred from observation (black) (Wang et al., 2021) and from our preferred dynamic rupture model (blue). (C) and (D): Observed displacements along the Line-of-Sight (LOS) of the ascending and descending Sentinel-1 interferogram, respectively (Supplementary Information Text S2). (E) and (F): Modeled surface displacements projected along the LOS. (G) and (H): residuals between the observed and modeled InSAR data.

**Table S1.** 3D Dynamic rupture model parameters of the preferred scenario. The upper part of the table lists the parameters used for the strong velocity-weakening rate-and-state friction law, the middle part describes the parameters used to compute the ambient regional stress state, and the lower part describes the parameters of the non-associated Drucker-Prager off-fault plasticity.

parameter	symbol	value	unit
Rate-and-state parameter, direct effect	$a$	0.01 ~ 0.02	-
Rate-and-state parameter, evolution effect	$b$	0.016	-
Characteristic state evolution distance	$D_{RS}$	0.020 ~ 0.121	m
Reference slip rate	$v_0$	$10^{-6}$	m/s
Reference friction coefficient	$f_0$	0.6	-
Initial slip rate	$V_{ini}$	$10^{-16}$	m/s
Initial state variable	$\theta_{ini}$	0.1	s
Weakening velocity	$v_w$	0.1	m/s
Strike	-	110	°
Dip	-	85	°
Rake	-	-10	°
Maximum compression orientation	$S_{Hmax}$	N78°E	-
Stress shape ratio	$\nu$	0.5	-
Prestress ratio	R0	0.52	-
Pore fluid pressure ratio	$\lambda$	0.37	-
Plastic cohesion	$C_{plast}$	$2 \times 10^{-4} \mu(z)$	Pa
Bulk friction coefficient	$C$	0.6	-
Relaxation time	$T_v$	0.05	s

**Figure S27.** Evolution of absolute on-fault slip rate [m/s] across the fault system. The animation is also available at <https://drive.google.com/file/d/1jFXLCprTuACPASxhw5gSDRK1rK0C6a1C/view?usp=sharing>.